THE JOURNAL OF PHYSICAL CHEMISTRY C

Article

pubs.acs.org/JPCC

Model-Free Unraveling of Supported Nanoparticles Plasmon Resonance Modes

Rémi Lazzari,*[,†,‡] Jacques Jupille,[†,‡] Rémi Cavallotti,[†,‡] and Ingve Simonsen[§]

[†]Sorbonne Universités, UPMC Univ Paris 06, UMR 7588, Institut des NanoSciences de Paris, 75005 Paris, France

[‡]CNRS, UMR 7588, Institut des NanoSciences de Paris, 75005 Paris, France

[§]Department of Physics, Norwegian University of Science and Technology (NTNU), NO-7491 Trondheim, Norway

Supporting Information

ABSTRACT: Plasmonics of Ag, Au, and Zn nanoparticles supported on $Al_2O_3(0001)$, $TiO_2(110)$, and ZnO(0001) substrates has been probed by surface differential reflectivity spectroscopy (SDRS) during vapor deposition growth. Parallel and perpendicular interfacial susceptibilities (ISs), or "optical thicknesses", which characterize only the dielectric response of the film, are derived from experimental spectra in p- and s-polarization using an inversion procedure based on Kramers–Kronig transform. The consistency of the approach is checked against sum rules. Plasmonic contributions are unraveled by decomposing ISs into damped oscillators and identified with the help of dielectric simulations of truncated supported spheres or spheroids. Beyond the common Drude behavior of Ag, Au, and Zn, the comparison between the three metals demonstrates the paramount role of interband transitions in the ISs profiles. While gold and silver show free electron plasmon modes, zinc exhibits polarization modes of bound electrons. However, despite those differences, the resonant modes that are identified herein are universal for supported particles. Particle shape, equilibrium aspect ratio, image field, polydispersity, and interface-induced damping are discussed by analyzing changes in frequencies, oscillator strengths, and broadenings. Deposit-induced band gap absorption for semiconductor substrate and switches from growth to coalescence regimes are evidenced. Static and dynamic coalescence are characterized by power law exponents as a function of particle size. Therefore, the unique framework that is proposed opens strong prospects in the optical characterization of growth, metal/semiconductor interfaces, and gas adsorption.

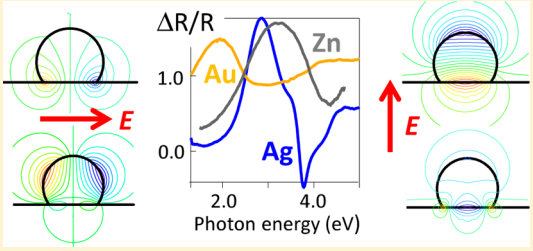

INTRODUCTION

Light is a nondestructive probe that can be operated at any temperature, either in vacuum or in gaseous and liquid environments. More specifically, the capability of UV–vis light to characterize via plasmon excitations metallic nano-objects[1−4] whose size is much smaller than the wavelength has boosted the development of nanoplasmonics. Plasmon polaritons of free-standing spheres or spheroids, which feature the most common cases, can be determined in the framework of the Mie theory with the extraordinary achievement that exact solutions exist even for the scattering of a plane wave in the nonretarded limit.[1,2,5] However, for manipulation, use, and device integration, particles are often deposited or grown on a substrate which dramatically affects the plasmonic response by break in symmetry of the particle environment[6−9] and shape due to wetting.[10−13] Even for a supported nanosphere, a rich set of plasmon resonances can be promoted by approaching the object from the substrate due to an increasing role of image field.[6,9,14] Neglecting retardation effects, a fair hypothesis for nanosized objects, the dipole excited by the incident light induces an image dipole which perturbs the local field seen by the particle which in turns excites a quadrupole mirrored in the substrate and so on. The phenomenon can be viewed as a cascade of multipole excitations or an hybridization phenomenon between the eigenmodes of polarization of the particle and of its mirror image.[7,9,15] Resonance line shapes and frequencies are quite sensitive to (i) the particle–substrate distance and image strength,[14,16−20] with a strong field enhancement within the gap[9,15,21] for nanospheres, (ii) substrate dielectric properties[8,22] which drive not only the image field but also the interfacial damping of the excitation,[23] (iii) the substrate/particle wetting and interface truncation,[10−13,24] and (iv) the coupling between objects.[25] Modelings have been performed using various frameworks[26,27] with spherical shapes[6,7,9,14,21] or more realistic profiles[3,11,12,19] showing the richness of the polarization modes.

However, the experimental analysis of optical responses of supported particles with integral methods, i.e., through measurements of Fresnel coefficients, is often hampered by substrate contributions. Mixing of parallel and perpendicular responses,[13] in particular in p-polarization, and substrate absorption blur dramatically the direct reading of the optical parameters. A similar issue is encountered while probing optically organic layer growth.[28,29] In an attempt to escape

Received: January 20, 2014
Revised: March 5, 2014
Published: March 7, 2014

   dx.doi.org/10.1021/jp500675h | J. Phys. Chem. C 2014, 118, 7032−7048

model-dependent approach of the optical spectra, we have recently proposed a theoretical methodology of recovering of layer dielectric properties.[30] It is based on Kramers−Kronig transforms in which the finite experimental range is completed by means of a spheroidal dipole modeling. The interaction of the light with the supported film is modeled on the basis of the excess field concepts, in terms of parallel $\gamma(\omega)$ and perpendicular $\beta(\omega)$ frequency-dependent interfacial susceptibilities (ISs).[31−33] These complex quantities have the meaning of "dielectric thicknesses" and characterize the optical absorption of the supported nanoparticles and the way the film polarizes[33] under the incident electric field. The ISs are given by the product of (i) the particle density ρ and the two components of the average polarizability tensor for supported nanoparticles or (ii) of the film thickness by its dielectric and loss functions for thin continuous films. Interfacial susceptibilities can be directly extracted from a combination of Fresnel coefficient measurements without the contribution of the substrate leading to a model-free description of the dielectric behavior of particles. The method was tested by means of synthetic surface differential reflectivity spectroscopy (SDRS) data in p- and s-polarization.

In the present work, experimental SDRS spectra are inverted[30] in order to decipher, along the two main directions of space, between the various ISs contributions, namely plasmon modes and bulk interband absorption. To do so, obtained ISs are decomposed as discrete sums of damped oscillators of frequencies ω_j, integrated strengths F_j, and damping Γ_j in a form known as a Kramers−Heisenberg representation:

$$\gamma(\omega) \simeq \gamma_{bk}(\omega) + \sum_j \frac{F_{\gamma,j}\Gamma_{\gamma,j}\sqrt{4{\omega_{\gamma,j}}^2 - {\Gamma_{\gamma,j}}^2}}{{\omega_{\gamma,j}}^2 - \omega^2 - i\omega\Gamma_{\gamma,j}}$$

$$\beta(\omega) \simeq \beta_{bk}(\omega) + \sum_j \frac{F_{\beta,j}\Gamma_{\beta,j}\sqrt{4{\omega_{\beta,j}}^2 - {\Gamma_{\beta,j}}^2}}{{\omega_{\beta,j}}^2 - \omega^2 - i\omega\Gamma_{\beta,j}} \quad (1)$$

Besides, background terms [$\mathrm{Im}(\gamma_{bk})$ and $\mathrm{Im}(\beta_{bk})$] are further introduced to account for bulk interband contributions (see Supporting Information). A similar decomposition was used to analyze the interplay between interband and plasmon peak contribution and their size dependence,[34−38] but the possibility of excitation of several modes has never been really accounted for in the description of band profile. In the same spirit as for adsorbed atoms[39] and in line to optical response of composites,[40] the representation of ISs eq 1 is based on the spectral decomposition of particle polarizabilities into eigenmodes of vibration of the electric charge of the object which is valid only in the undamped regime.[41] The obtained modes have a purely geometric nature and appear at given values of the particle dielectric function. For supported particles, the decomposition has been derived theoretically for supported full spheroids[6] but has never been generalized to any supported shape as it has been done for 3D case of composites.[40] Therefore, the application of eq 1 to actual data sets aside modes mixing due to nearly degenerated resonances and overlapping contributions between bulk absorption and plasmon resonances. Moreover, all parameters must be interpreted as average values since eq 1 assumes that polydispersity and spatial heterogeneity keep the intrinsic nature of the monodisperse and isolated object. ω_j is determined by (i) particle aspect ratio (diameter/height, D/H) and (ii) density of objects via local field effects due to particle−particle coupling;[41] F_j is mainly governed by particle shape, and Γ_j is sensitive to both material absorptions and inhomogeneous broadening due to polydispersity.[42,43]

In the plasmonic response of metals, a central issue is the mixing of free and bound electrons in resonant modes. Therefore, it has been chosen to analyze three metals, silver Ag($4d^{10}5s^1$), gold Au($5d^{10}6s^1$), and zinc Zn($3d^{10}4s^2$), which have filled d-shells and similar s-electron Drude behaviors but differ from the position of the interband absorption threshold which is red-shifted progressively from 4 eV to below 1.5 eV (see Supporting Information). They are representative of different conformations of screening of free electrons by bound electrons. Their dielectric functions (Ag,[44−46] Au,[44,45] and Zn;[47] Figure 1 of Supporting Information) have been systematically decomposed into Drude and interband components:

$$\epsilon(\omega) = \epsilon_f(\omega) + \epsilon_{ib}(\omega) = \epsilon_\infty - \frac{{\omega_f}^2}{\omega^2 - i\Gamma_f\omega} + \epsilon_{ib}(\omega) \quad (2)$$

Notably, a cut at a given value of Real(ϵ) shows that (i) for silver plasmonic resonances are in an energy range that is well below that of interband transitions, (ii) for gold resonances should be much closer to interband transition, and (iii) for zinc resonances are expected within the higher energy tail of the interband transition; moreover, in this last case, the same real value can be found at two different energies. Finally, the three different substrates used herein, alumina Al_2O_3, zincite ZnO, and titania TiO_2, display different dielectric behaviors[44,48] (see Figure 2 of ref 30). Alumina is an archetype of wide band gap oxide with a nearly constant dielectric function and a lack of absorption in the UV−vis range. In contrast, wurtzite and rutile are wide band gap (E_g = 3.4 and 3 eV) semiconductors.

The principle of the experiment is to record SDRS spectra of growing metal/oxide systems. Equations giving the reflection coefficients are then inverted[30] to obtain parallel and perpendicular ISs based on the Kramers−Kronig transform between real and imaginary parts. Since most of the resonant behavior is grasped by the Kramers−Kronig transform, the validity and accuracy of the inversion process do not depend heavily on the morphology of the deposit.[30] ISs are then decomposed into oscillators (eq 1) whose positions in energy, strengths, and widths are determined. The nature and characteristics of modes are discussed by comparison with simulations performed using the GranFilm code[49,50] on particles modeled by representative truncated spheres or spheroids. Each metal is analyzed to highlight the effects of interband transitions and demonstrate the composite nature of the observed bands. Information regarding the growth process of the films and the electronic structure of the interface are also deduced from shifts in frequency and deposit-induced band gap absorption. Finally, the consistency of the approach is checked *a posteriori* through sum rules applied to ISs.[51]

EXPERIMENTAL SECTION

Experiments have been carried out in a vacuum vessel (base pressure of 5×10^{-9} Pa) which consists in a preparation chamber where films are deposited and an analysis chamber equipped with an X-ray photoemission spectrometer (XPS) and a low-energy electron diffraction device (LEED). Epipolished alumina Al_2O_3(0001) substrates were prepared *in*

dx.doi.org/10.1021/jp500675h | J. Phys. Chem. C 2014, 118, 7032−7048

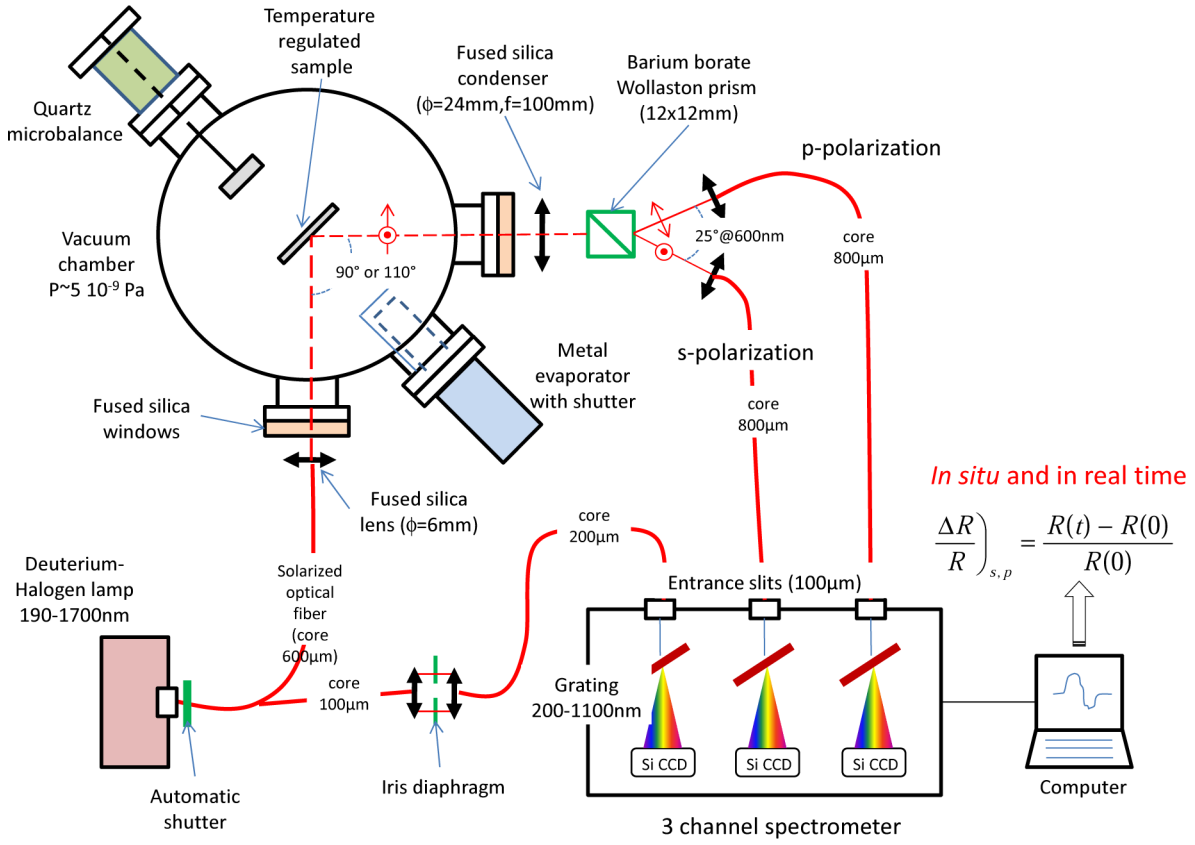

$$\left(\frac{\Delta R}{R}\right)_{s,p} = \frac{R(t) - R(0)}{R(0)}$$

Figure 1. Schematics of the surface differential reflectivity spectroscopy setup. Optical fibers are represented by bold red lines and free path of light by dotted red lines. All optical elements are made of fused silica to enhance UV transmission. The reflected light is split into its s- and p-polarization components by a Wollaston prism and corrected from source drift (see text).

situ by annealing at high temperature ($T \geq 1200$ K) under oxygen partial pressure ($p = 5 \times 10^{-4}$ Pa). Clean TiO_2(110) and ZnO(0001)-Zn surfaces were obtained by cycles of Ar^+-ion sputtering (kinetic energy 800 eV) followed by vacuum annealing ($T \simeq 1100$ K). Such a preparation led to bulk reduced conducting titania substrate as seen from its dark blue color. The final surface contamination was below the detection limit of XPS analysis. All substrates displayed a sharp (1 × 1) LEED pattern after thermal treatment. SDRS spectra have been acquired during metal (Ag, Au, and Zn) vapor deposition from a heated crucible with a deposition rate in the range 0.04−0.08 nm/min as calibrated by a quartz microbalance. All depositions were performed in a pressure range in the high 10^{-8} Pa on a substrate held, either at room temperature for Ag and Au or at 100 K for Zn to obtain a sizable condensation coefficient.[52] The growth of Ag, Au, Zn/Al_2O_3, Ag/ZnO, and Au/TiO_2 has been optically studied up equivalent thicknesses of around 2 nm.

SDRS consists in recording the relative variation of the sample reflectivity $\Delta\mathcal{R}/\mathcal{R}$ during metal vapor condensation. The optical setup (Figure 1) is specially designed to record simultaneously the two polarization states s and p of light, i.e., with the electric field normal and parallel to the incident plane. It involves a three-channel spectrometer (from Avantes) made of three fixed identical dispersing grating benches and CCD Si-array detectors. The accessible spectral range from about 200 to 1000 nm is limited by the detector response and optical bench transmission. The resolution given by the spectrometer entrance slit and the grating groove density is around 5 nm. Wavelength-pixel calibration was performed at factory and checked with both Hg-lamp and deuterium sharp emission lines. Because of the wide wavelength bandwidth used, high-order diffraction peaks on a given pixel are suppressed by a wedge coating on the detector. The optical benches of symmetric Czerny−Turner type are designed to enhance UV signal through grating blazing, internal lens condenser, and special UV coatings. Most of the beam path during measurement is guided into solarized silica optical fibers to keep the UV transmittance. The light emitted by a dual deuterium/halogen source is focused on the entrance of a single-core Y-shaped optical fiber. The beam in the first branch of the Y-fiber, after having been diaphragmed to avoid detector saturation, is used to correct the two other channels from lamp drift. The light in the other branch is focused on the sample through a silica viewport at an incident angle $\theta_0 = 45°$ or 55° fixed by the chamber flanges. A manipulator which can be cooled down at ∼100 K by circulating liquid nitrogen allows positioning the sample on the beam path. The reflected light is collected by a convergent silica condenser and sent onto an α-BBO (barium borate) Wollaston prism with a symmetric splitting angle of 25° at $\lambda = 600$ nm. This results in the separation of the two states of polarization s and p into two beams. Barium borate is preferred over calcite because of its better transmittance below $\lambda = 350$ nm. The splitting angle of the two beams is nearly constant over the spectral range down to $\lambda \sim 300$ nm, below which it increased up to 45° leading to loss of UV intensity. The polarization efficiency is higher than 99%. The two beams are collected by lenses into an optical fibers plugged onto the entrance slits of two other channels of the grating analyzer.

Despite the low reflectivity of the oxide substrates, the typical integration time is in the range of 10 ms thanks to the high

dx.doi.org/10.1021/jp500675h | J. Phys. Chem. C 2014, 118, 7032−7048

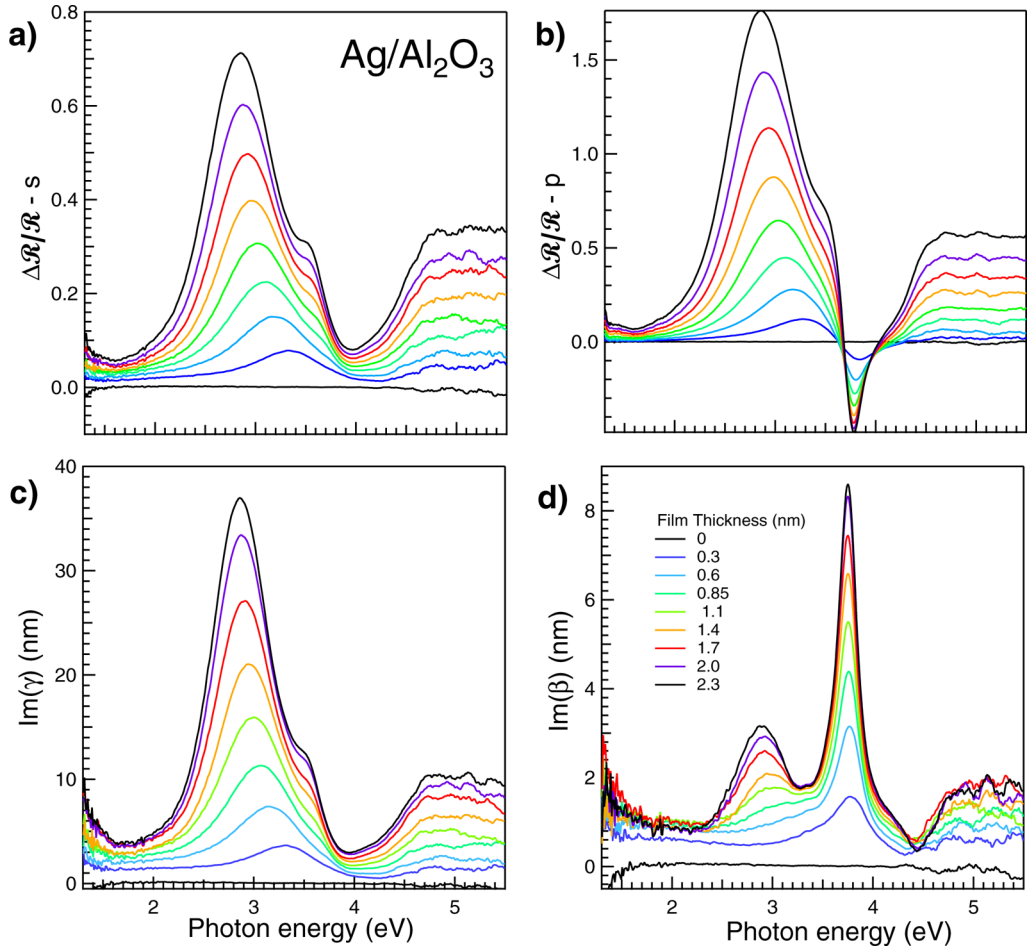

Figure 2. Silver on alumina: experimental SDRS spectra recorded during growth in (a) s- and (b) p-polarization. Corresponding inverted imaginary parts of the interface susceptibilities: (c) parallel IS Im(γ) and (d) perpendicular IS Im(β). Film thickness is given in the legend.

sensitivity of the CCD silicon detector. When the evaporation rate is slow, as in the present work, hundreds of spectra can be averaged to reach a frequency of acquisition of around 10 actual spectra per minute. A smoothing over a moving windows of a few pixels among the 1700 active pixels can further enhanced the statistics without loosing the intrinsic resolution. An overall signal stability of $\Delta\mathcal{R}/\mathcal{R} \simeq 2 \times 10^{-3}$ can be achieved in the wavelength range of λ = 300−900 nm. Bare spectra are corrected from dark signal, source drift and normalized by an average of 1 decade of acquisitions before evaporation in order to get the actual differential data.

SILVER ON ALUMINA AND ZINCITE

A 2.5 nm thick Ag/alumina film and a 1.8 nm thick Ag/zincite films have been grown in similar conditions. The experimental SDRS spectra recorded during growth are displayed in the upper panels of Figures 2 and 3 for s- and p-polarizations of the incident light. As shown in the lower panels of Figures 2 and 3, the inversion process[30] is stable in the two cases and provides positive imaginary parts of the ISs, except close to the band gap edge of ZnO for the thickest films. Because of the Volmer−Weber growth of Ag, the optical reflection is dominated by the sharp plasmon resonances which characterize 3D nanoparticles. In the case of ZnO, they are clearly disentangled from the band gap features seen in the raw SDRS spectra. The absorption above ∼4 eV is the signature of the silver interband transitions. For thickest deposits, ISs scale up to several tens of nanometers, a value much higher than the film thickness, which explains the failure of the long wavelength approximation in describing the dielectric response of supported nanoparticles.[30] Distinct behaviors are clearly observed in the two directions of space. Along the direction parallel to the substrate (Im(γ), Figures 2c and 3c), an intense red-shifting band (from 3.2 to 2.8 eV and from 2.6 to 1.3 eV for alumina and zincite, respectively) with a shoulder on the higher energy side is observed. Two less intense peaks appear along the perpendicular direction (Im(β), Figures 2d and 3d): one at nearly constant energy (3.8 eV for both substrates) and the other that is red-shifted (3−2.8 eV for alumina, 3−1.5 eV for zincite). Most importantly, the inversion unambiguously distinguishes the parallel and perpendicular components of the optical response of supported silver and reveals components hidden in bare spectra.

Mode Assignment, Particle Shape, and Substrate Effects. To identify the different contributions to the plasmonic response of Ag/Al_2O_3 and Ag/ZnO, Im(γ) and Im(β) are fitted on the basis of the spectral representation (eq 1) for two selected thicknesses for alumina (2.3 nm) (Figure 4) and zincite (0.85 nm) (Figure 5). Background terms Im(γ_{bk}) and Im(β_{bk}) nicely reproduce bulk interbands (see Supporting Information). A minimum of two oscillators is needed to account satisfactorily for Im(γ) and Im(β) line shapes in the case of Ag/alumina. Regarding Ag/zincite, fits are achieved with only one parallel component.

dx.doi.org/10.1021/jp500675h | J. Phys. Chem. C 2014, 118, 7032−7048

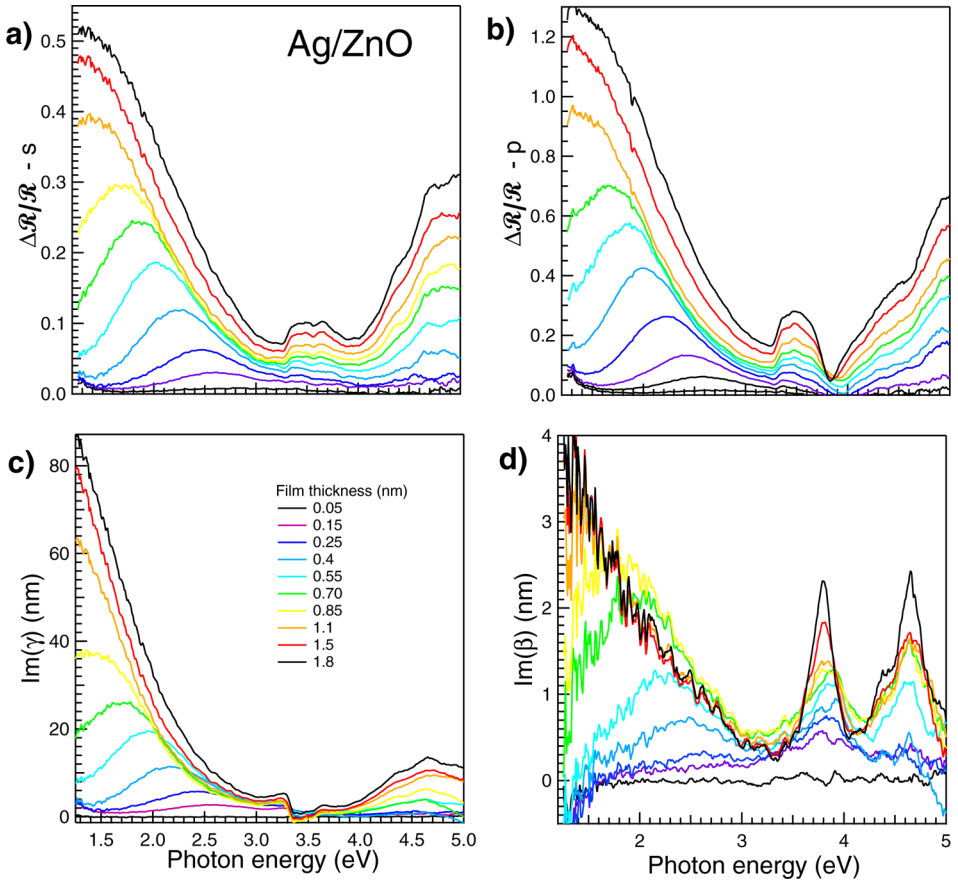

Figure 3. Silver on zincite: same legend as for Figure 2. Notice the differences with the alumina substrate, in particular the positions of the plasmon features and the signature of the band gap in the reflectivity data which is partly removed by the inversion process (see text).

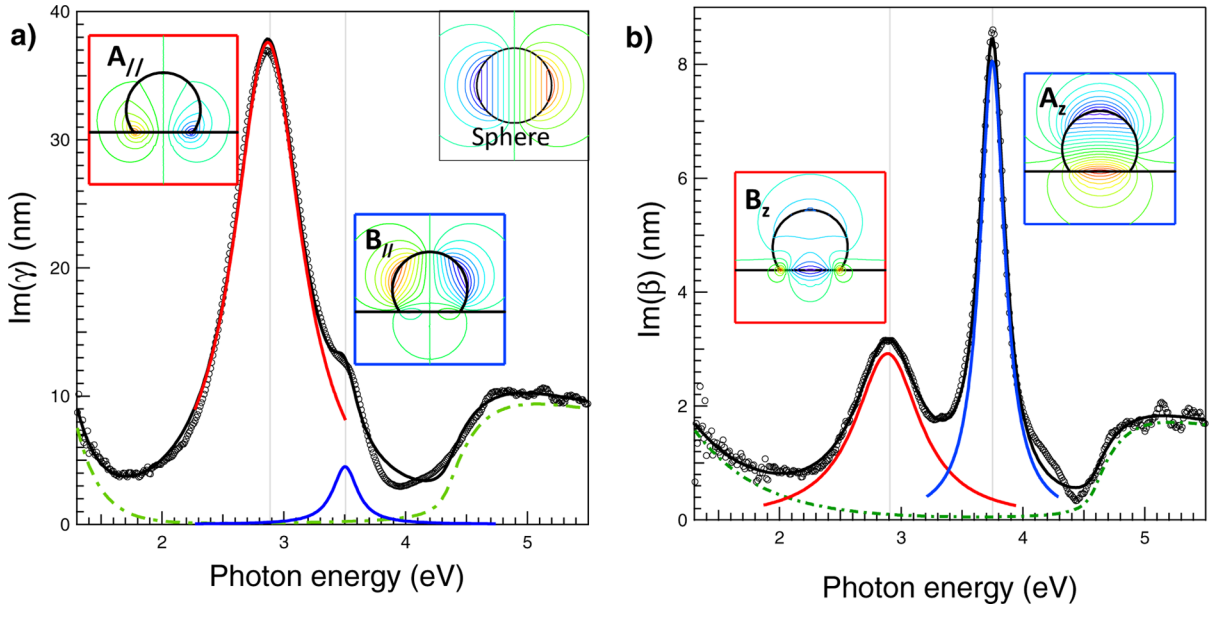

Figure 4. Silver on alumina: damped oscillator decomposition of IS imaginary parts of the 2.3 nm thick Ag/alumina spectrum (Figure 2). Experimental points (black circles) are overlaid with the fit (black continuous line), the various plasmon components (red and blue lines), and a background defined from the interband absorption in silver (dot-dashed green line) (see text). Calculated maps of potential of the associated eigenmodes of charge vibrations are shown in the inset (see text) for the expected equilibrium particle shape. The upper-right inset in the figure a shows the Frölich mode of the isolated full sphere. The increase of signal below 1.5 eV comes from spurious light.

Dielectric simulations of supported truncated spheres[10,21,33,49,53] or spheroids[11] provide a relevant tool to interpret this phenomenological decomposition and assign the observed features. The truncated sphere does correspond to the

dx.doi.org/10.1021/jp500675h | J. Phys. Chem. C 2014, 118, 7032−7048

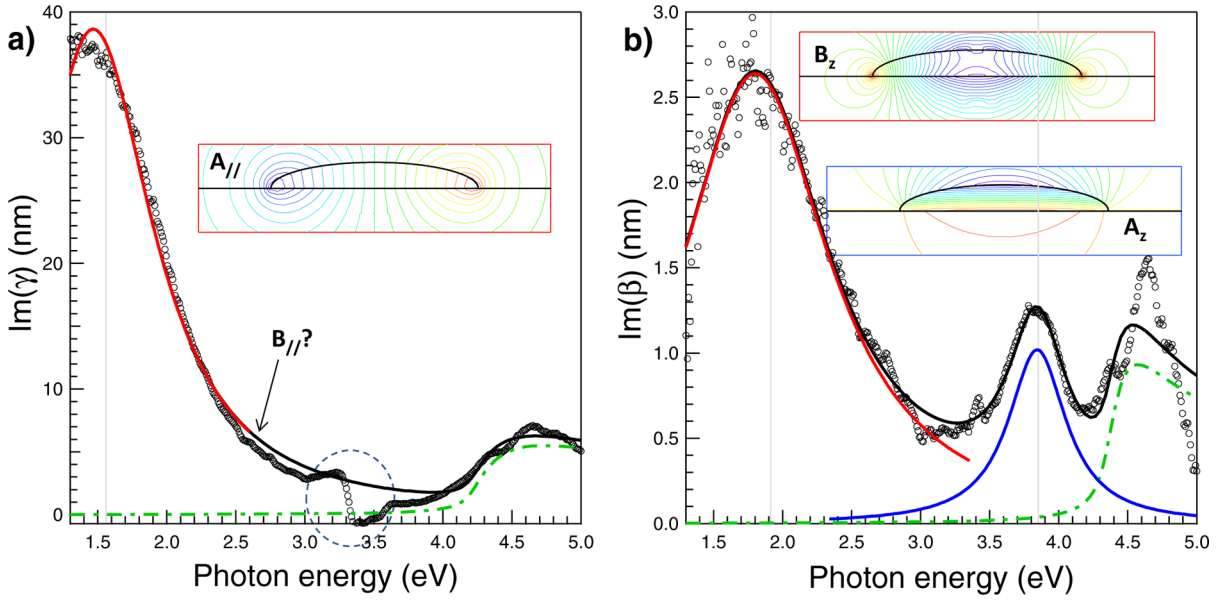

Figure 5. Silver on zincite: same legend as for Figure 4 but for a 0.85 nm thick silver film on zincite. Notice the feature around the band gap of ZnO which is not accounted for in the simulation.

expected equilibrium shape of a liquid or a metal with low surface energy anisotropy[43] while the truncated spheroid offers enough flexibility to describe coalescence-induced flattening.[54] In the quasi-static approximation, a fair hypothesis for nanosized objects, eigenmodes of polarization[12,41] are found using a multipolar spherical or spheroidal expansion of the potential in the limit of undamped media. The procedure accounts for the influence of the substrate and for the particle−particle coupling.[12,41] Since aspect ratios (diameter/height, D/H) drive to a large extent the plasmonic behavior,[2] particles are modeled by equilibrium shapes previously determined (see inset of Figure 6). Ag/Al_2O_3 particles and 2D flat-top Ag/ZnO particles[55−57] are mimicked by truncated spheres whose contact angle is 125° (refs 42, 43, and 58) and by truncated oblate hemispheroids (D/H = 8), respectively. Simulations of the positions and integrated intensities of the various modes are performed with the GranFilm code[49,50] using tabulated bulk dielectric functions for metals,[44,45] alumina,[44] and ZnO[48] without any finite-size corrections. The characteristics of the modes displayed in Figure 6, which show a sizable effect of the particle shape and substrate, are in good agreement with the components obtained by fitting the inverted spectra with oscillators (Figures 4 and 5). The assignment of the main experimental modes stems from their positions in energy and relative strengths. Corresponding polarization charges are mapped out in insets of Figures 4 and 5 through potential lines at the resonance.

The plasmonic response of Ag/alumina is dominated by two modes parallel to the substrate ($A_\parallel$ and $B_\parallel$) and two modes perpendicular to the substrate (A_z and B_z).[12,41] The inversion[30] clearly reveals A_z, a component otherwise hidden in the raw SDRS spectra. Only three modes ($A_\parallel$, A_z, B_z) are reasonably active for the flat Ag/ZnO particles since $B_\parallel$ is hardly discernible in the tail of Im(γ) (Figure 5a). Oscillator strengths of other components are much lower (Figure 6, truncated sphere case, and next section on Au). Similarities of the equipotential patterns in truncated spheres (Ag/Al_2O_3) and spheroids (Ag/ZnO) lead to their common mode labeling. In the 3D representation of the polarization charges, $A_\parallel$ and $B_\parallel$

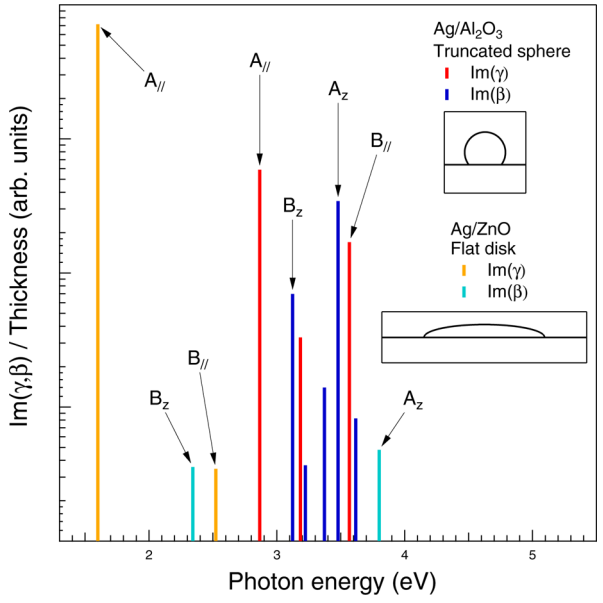

Figure 6. Absorption eigenmodes for a truncated sphere (Ag/Al_2O_3) and a flat spheroidal shape (Ag/ZnO) (shown in inset). The ticks represent the integrated oscillator strengths normalized by the particle volume. The two most intense modes for each direction are labeled by $A_\parallel$, $B_\parallel$, A_z, and B_z, and their patterns of charge vibration are shown in Figures 4 and 5. The left scale is logarithmic.

(Figures 4a and 5a), which are activated by both p- and s-polarized light, have a symmetry plane normal to the parallel component of the electric field. In contrast, A_z and B_z (Figures 4b and 5b), which are actived only in p-polarization by the normal component of the electric field, have a rotational symmetry along the surface normal. The two main modes ($A_\parallel$, A_z) exhibit a strong dipolar character; $B_\parallel$ and B_z show instead some quadrupolar character in their polarization charge pattern with some charge pinning at the top of the particle and the interface.

dx.doi.org/10.1021/jp500675h | J. Phys. Chem. C 2014, 118, 7032−7048

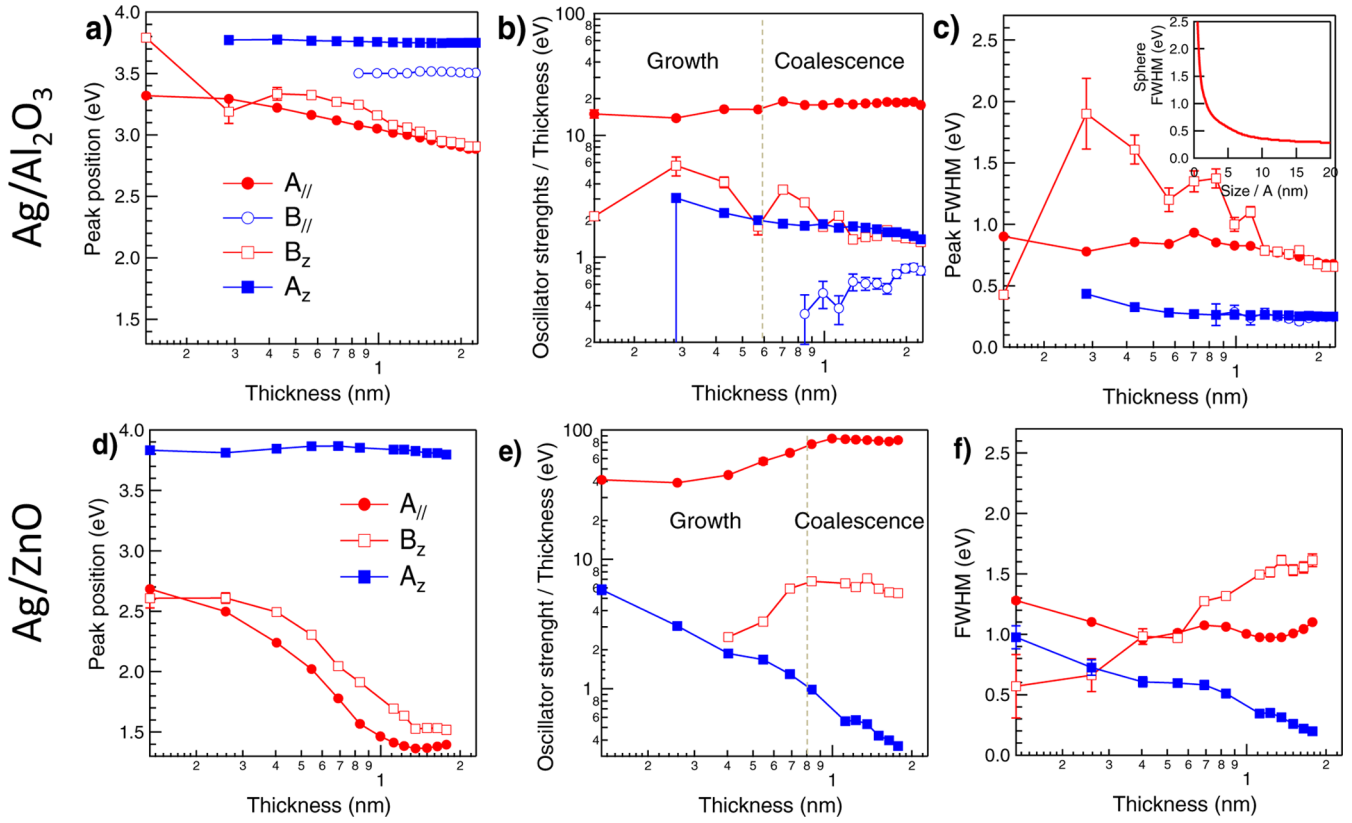

Figure 7. Silver on alumina (top panels a, b, c) and silver on zincite (lower panels d, e, f): evolution upon film growth of (a, d) the positions ω_j, (b, e) the oscillator strengths F_j normalized by the film thickness t, and (c, f) fwhm of the oscillator components of Figures 4 and 5. Circles (squares) correspond to Im(γ) (Im(β)). Mode labels correspond to potential maps of Figures 4 and 5. The inset in (c) shows the effect of size broadening on the calculated fwhm of the full embedded sphere resonance (see text). Vertical dotted lines in (b, c) highlight the transition from growth to coalescence.

Oscillators Strengths and Frequency Shifts To Derive Shape and Growth Modes. Fitted oscillator parameters of the main plasmonic modes of Ag/alumina (Figure 7a–c) and Ag/zincite (Figure 7d–f,) involve frequencies ω_j (Figure 7a,d), integrated oscillator strengths F_j/t (normalized by the film thickness t) (Figure 7b,e), and full width at half-maximum (fwhm) related mainly to Γ_j (Figure 7c,f). The intensity range in which a given parameter is represented is always the same throughout the present work, for comparison.

Although showing similar trends, the two systems exhibit drastic differences that are now explored. Since the normalized oscillator strength F_j/t is driven only by the particle shape, the main $A_{\parallel}$ mode is a fair reference. For Ag/alumina, it faintly evolves up to $t \simeq 0.6$ nm and is constant above (Figure 7b), which indicates a growth at constant density followed by coalescence at a constant shape likely close to equilibrium, in agreement with previous fits of optical spectra with truncated sphere modeling.[42,43,54,58] Added to the poorly evolving broadening that reflects D/H polydispersity[42,43] (Figure 7c), the observation confirms a self-similar behavior of the coalescence process.[43,59] The lower energy at which appears the $A_{\parallel}$ mode of Ag/zincite (Figure 7b,e) and its higher intensity (Figure 7a,d) points to higher values of D/H relative to Ag/alumina. Moreover, the increase in F_j/t up to $t \simeq 1$ nm (Figure 7e) characterizes a continuous increase in D/H. Consistently, the higher splitting in F_j/t of the $A_{\parallel}$ and A_z modes[2] demonstrates the formation of flatter clusters on ZnO than on alumina.

In a pure dipole picture, in the limit of small damping and in a mean field approximation,[12,33,41] particle interactions shift the mode position $\omega_j(\rho)$ according to

$$\omega_j(\rho) = \omega_j(\rho = 0) \pm S\sqrt{\rho}F_j \quad (3)$$

where ρ is the particle density, $\omega_j(\rho = 0)$ is the mode frequency of the isolated object which is a function of the particle shape and therefore of F_j/t, and $S > 0$ is a constant prefactor. S depends on the dielectric functions of the materials which are nearly constant in the spectral range under concern. The trend given by eq 3 is obeyed in Figure 7: the higher F_j, the stronger the slope of the shift. Parallel modes are red-shifted (− sign in eq 3) and perpendicular modes are blue-shifted (+ sign in eq 3) except A_z, maybe because of the presence of the nearby strong $A_{\parallel}$ mode. When coalescence occurs at constant F_j/t or particle shape, $\omega_j(\rho = 0)$ is constant; therefore, the power law behavior $\omega_j(\rho) \propto F_j^k$ leads to $\rho \propto F_j^{2k-2} \propto t^{2k-2}$ and then, by assuming a sticking coefficient of silver close to one,[43] to the particle size $D \propto (t/\rho)^{1/3} \propto t^{1-2/3\kappa}$. The value of $\kappa = 0.5$ derived by applying the formula to the main $A_{\parallel}$ mode of Ag/alumina results in a power law $D \propto t^{0.65\pm0.1}$, in agreement with $D \propto t^{0.55}$ found by directly fitting optical spectra[43] and ascribed to a dynamic process of coalescence involving mobile clusters.[43,60] For Ag/zincite, $\kappa = 0$ and $D \propto t^{1\pm0.1}$. In contrast with Ag/alumina, this linear behavior t^1 points to static coalescence in agreement with numerical simulation, scaling arguments, and analytic models of the phenomenon.[61,62] Indeed, silver wets rather well ZnO polar

dx.doi.org/10.1021/jp500675h | J. Phys. Chem. C 2014, 118, 7032–7048

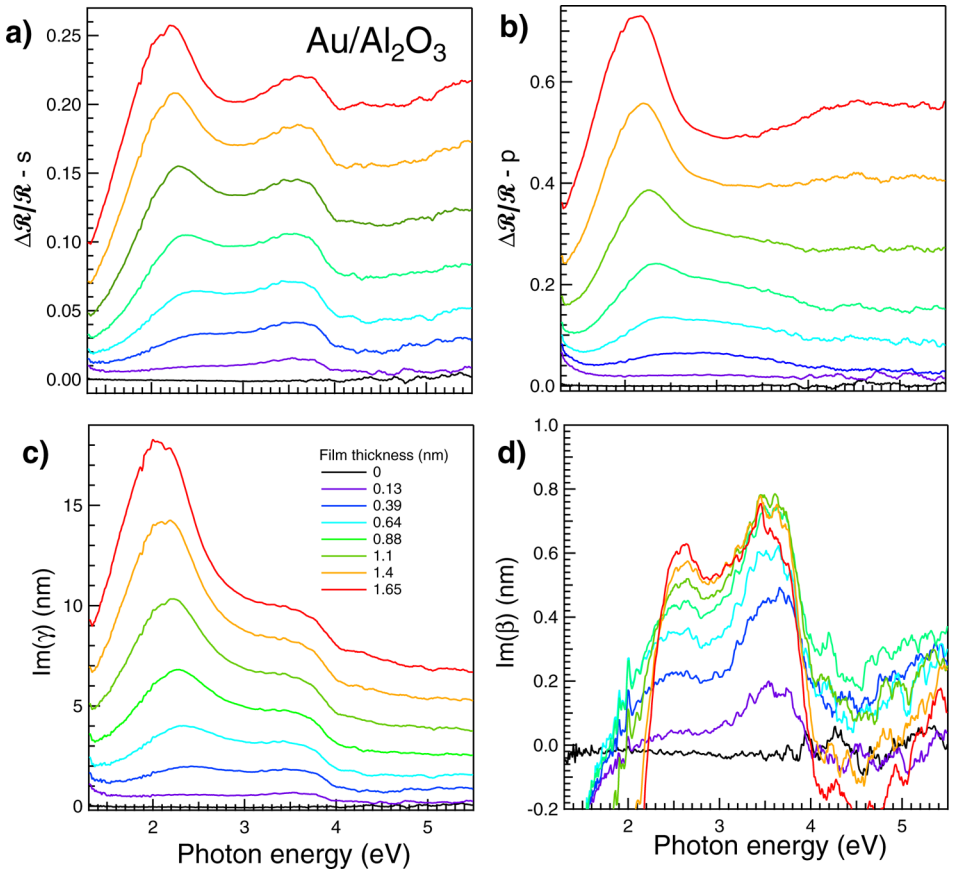

Figure 8. Gold on alumina: same legend as Figure 2. Notice the difference of intensities between the two ISs.

faces which is partly due to long-range coincidence lattices as observed by X-ray diffraction.[56,57]

The higher aspect ratio and the better wetting of Ag/ZnO with respect to Ag/alumina, as well as the static vs dynamic coalescence, that are demonstrated herein are consistent with previous studies and fits of optical spectra. However, the oscillator decomposition used in the present work is a direct method which is "free" of any modeling.

Mode Broadening. The broadening of $A_{\parallel}$ and B_z with respect to A_z and $B_{\parallel}$ (Figure 7c,f) is partly extrinsic because, with higher oscillator strengths, these modes are more sensitive to the inherent polydispersity of shape and particle−particle electrostatic coupling.[42,43] The phenomenon has also an intrinsic basis since the polarization charges of $A_{\parallel}$ and B_z are localized at the interface which make them more prone to chemical interface damping.[22,23] For instance, silver nanoparticles on/in SiO_2 show a noticeable size-dependent increase of the plasmon peak width compared to free clusters.[63,64] Based on the Frölich plasmon mode of the spherical particle (Figure 4a), this was assigned to a decoherence induced among the collective motion of electrons by adsorbate or interface states.[64] Chemical interface damping was also demonstrated with the technique of persistent hole burning.[65] But the role of charge polarization pattern has never been highlighted experimentally in the context of supported objects.

The decrease in peak width with deposited thickness stems from the variation of electron mean free path as a function of the particle size D due to surface scattering;[2,63,66−70] it is usually accounted for by a D-dependent damping in the Drude part of the dielectric constant:

$$\epsilon(\omega, D) = \epsilon_b(\omega) + \frac{{\omega_f}^2}{\omega^2 + i\omega\Gamma_f} - \frac{{\omega_f}^2}{\omega^2 + i\omega\Gamma_D}$$
$$\text{with } \Gamma_D = \Gamma_f + 2Av_F/D \quad (4)$$

where $\epsilon_b(\omega)$ is the bulk dielectric function, Γ_f the bulk Drude damping, v_F the Fermi velocity, and $A \simeq 1$ a constant which may vary with the environment.[63,70] However, for metals, the contribution of bound electrons modifies the bandwidth of the resonance. In the case of the Frölich mode of an embedded sphere, the fwhm can be determined by calculating the sphere polarizability as a function of D:[71]

$$\alpha(\omega, D) \propto \frac{\mathrm{Im}[\epsilon(\omega, D)]}{(\mathrm{Re}[\epsilon(\omega, D)] + 2\epsilon_e)^2 + \mathrm{Im}[\epsilon(\omega, D)]^2} \quad (5)$$

For $\epsilon_e = 2.12$, average between alumina and vacuum, an absorption close to 3 eV is found. For embedded spheres larger than 20 nm in size, its fmwh tends to 0.3 eV[2,63] ($A \simeq 1$), a value identical to the high thickness limit 0.25 eV of the A_z and $B_{\parallel}$ modes (Figure 7c,f). Indeed, these modes are poorly sensitive to inhomogeneous broadening,[12,42] and their charge patterns resemble that of a sphere (inset of Figure 4a). In contrast, the bandwidths of $A_{\parallel}$ and B_z do contain a sizable contribution of polydispersity, in particular of shapes,[42] since their patterns of polarization are influenced by truncation and substrate. In previous work,[42,43] using Gaussian convolution description of broadening, extra inhomogeneous contribution was estimated in the range of 0.3 eV for the $A_{\parallel}$ mode, which confirms the present finding. Undoubtedly, intrinsic size-limited broadening should be field direction- and mode-dependent.[68] But

dx.doi.org/10.1021/jp500675h | J. Phys. Chem. C 2014, 118, 7032−7048

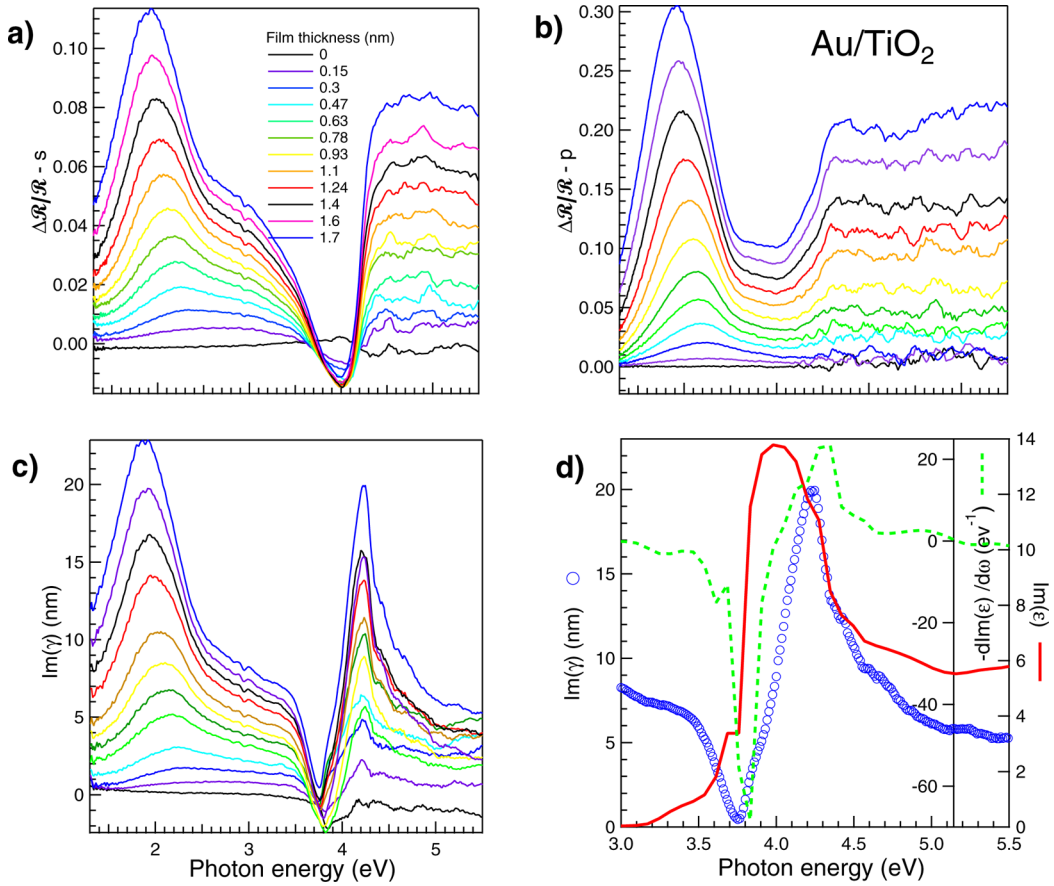

Figure 9. Gold on titania: same legend as Figure 2. Part d shows a comparison between the imaginary part of the bulk dielectric function ϵ of TiO_2 (bold red line), the opposite of its derivative (dotted green line), and the band gap feature of the last spectrum of part a (blue circles).

developing a quantum approach[68] of surface plasmon broadening for arbitrary shape objects is far from being simple. It is restricted to simple objects such as sphere for which the band structure of free electrons can be calculated. For other shapes, only classical geometrical approaches are available.[70] Finally, it is worth noticing in passing that the bandwidth of the isolated sphere resonance fwhm $\propto D^{-0.7}$ (inset of Figure 4) does not follow the size dependence of the free electron trend fwhm = $2\Gamma_D \propto D^{-1}$ because of the strong interplay with bound electrons in silver.[63] This ascertainment pinpoints the pitfall of the determination of A parameter (eq 4) from peak width measurements.

THE ROLE OF INTERBAND TRANSITIONS IN GOLD

Experimental SDRS spectra were recorded during the growth of Au/alumina (Figure 8, upper panels) and Au/rutile (Figure 9, upper panels). Gold differs from silver by strong interband transitions at 2.64 and 3.75 eV.[45,72] Mixtures of free and bound electrons excitations are expected.

Gold on Alumina. The inversion of SDRS spectra allows the extraction of the perpendicular Im(β) contribution (Figure 8d) which is hidden in the raw SDRS spectra because of an unfavorable ratio of intensity between parallel and perpendicular directions. The inversion starts being unstable above a thickness of ~1.5 nm[30] because of the energy closeness of the features, but this does not entail the following discussion. ISs are characterized by (i) a broad Im(γ) feature that is redshifting between 2.4 and 1.8 eV, (ii) a Im(β) peak ca. 2.6 eV, and (iii) a broad bump/kink between 3 and 4 eV. As in the case of silver, dielectric simulations[49,50] provide a guideline for the determination of the nature of the observed modes (Figure 10a,b). Particles are represented by truncated spheres whose aspect ratio is similar to that of Ag particles (owing to the poor Au/alumina wetting[73,74]) with bulk dielectric parameters. By accounting only for the real part of the dielectric function of gold, i.e., by suppressing the damping due to the imaginary part, the four $A_{\|}$, $B_{\|}$, A_z, and B_z modes previously introduced show up plus two extra features $C_{\|}$ and C_z located between 2.3 and 2.7 eV (inset of Figure 10b). (These were marginal in the case of silver and were not shown.) The decomposition between Drude and interband components of the gold dielectric function based on refs 45 and 72 (Figure 1b of Supporting Information) allows assigning those features to free electron modes; indeed, they do not appear when accounting only for the contribution of bound electrons (dotted line in Figure 10). However, when using the full dielectric function of gold, modes are considerably broadened due to their positioning close to the tail of interband transitions at 2.64 eV.[45,72] The intensity ratio A_z/B_z is reversed, and the mode $B_{\|}$ appears as a shoulder. Despite that broadening, the comparison with experimental findings (Figure 8) allows assigning (i) the main peak in Im(γ) to a dominant $A_{\|}$ component combined with $B_{\|}$ and $C_{\|}$ contributions, (ii) the Im(β) feature close to 2.6 eV to a mixture of A_z and B_z modes and interband absorption, and (iii) the bump between 3 and 4 eV to bulk interband transitions[72] (see Im(ϵ) and Im($1/\epsilon$) in Figure 1 of Supporting Information).

dx.doi.org/10.1021/jp500675h | J. Phys. Chem. C 2014, 118, 7032−7048

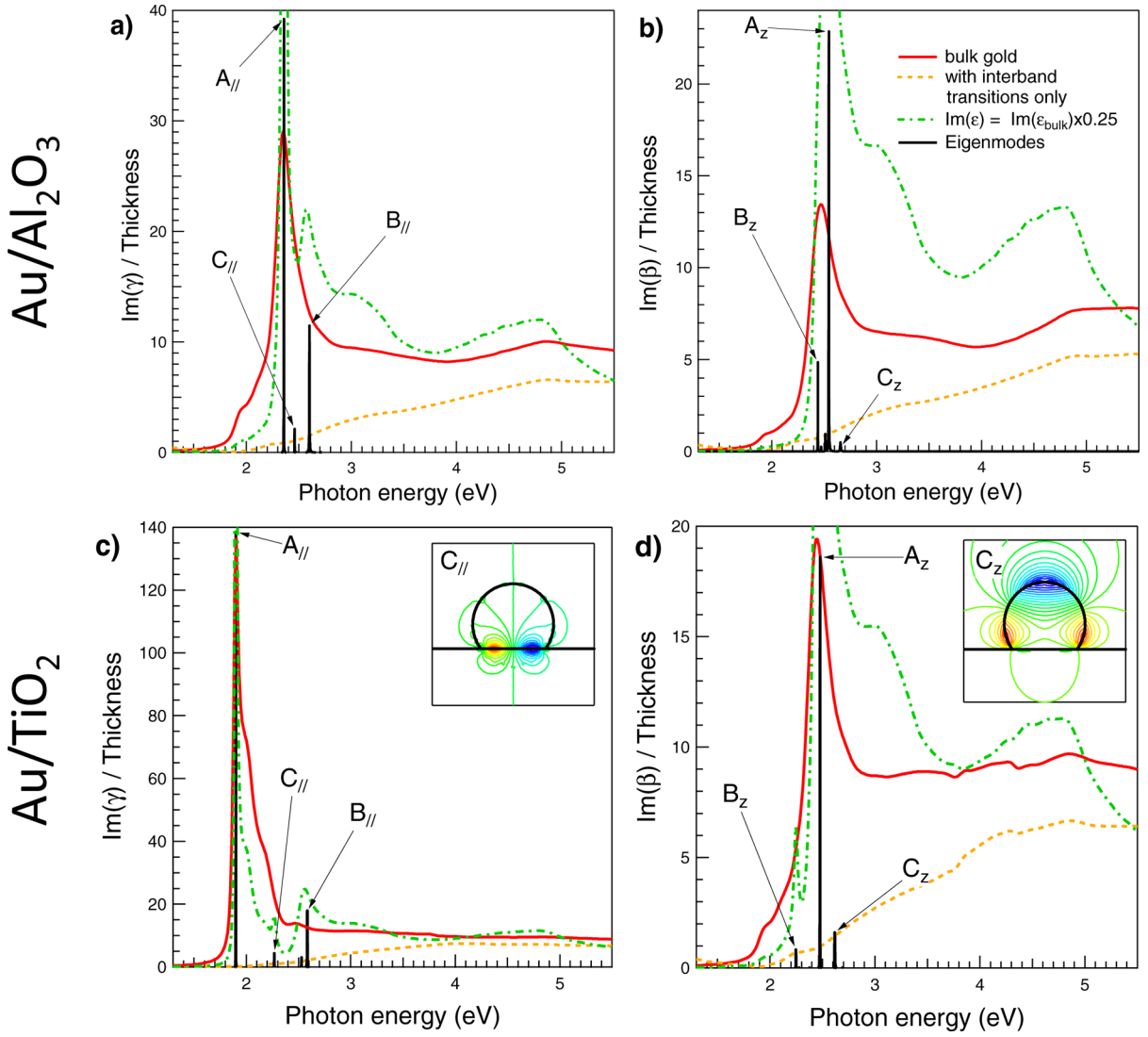

Figure 10. Gold on (a, b) alumina and (c, d) titania: simulated imaginary parts of the (a, c) parallel IS Im(γ) and (b, d) perpendicular Im(β) IS for a truncated sphere shape accounting either (i) for all the components of the gold dielectric function (continuous red lines), (ii) only a fraction of it (25%, dash-dotted green line), or (iii) only for the interband transition contribution (dotted orange lines). The used decomposition in free and bound electrons of the dielectric function of gold is shown in Figure 1b of the Supporting Information. The black tick positions and heights stand for the predicted frequencies and integrated strengths of the prominent modes of absorption; the scale is linear and arbitrary. Their labeling is similar to that of Figure 6, except for the new $C_{\parallel}$ and C_z modes whose patterns of charge localization are shown in the insets.

The spectral decomposition undertaken in the same spirit as in the case of silver (Figures 4 and 5) by parametrizing interband transitions[72] (see Supporting Information) leads to a poor matching with experiments (not shown) which might arise from either (i) mode mixing and breakdown of the spectral decomposition eq 1 based on decoupling between bound and free electrons or (ii) size-dependent electronic structure of bound electrons.[75,76] Good fits could be obtained but at the expense of meaningless variations of the parameters of the critical point transitions[72,77] (see Supporting Information). Therefore, a pragmatic approach was followed by fitting Im(γ) up to ~3.3 eV with a parabolic background (inset of Figure 11b) that mimics the tail of the d-electrons contribution (Figure 10 dotted line) and a unique oscillator ($A_{\parallel}$) whose parameters are gathered in Figure 11. Regarding its limit of fwhm in the range where size-limited broadening is negligible (eq 4), the extra broadening of 0.6 eV found with respect to the Frölich resonance of an embedded gold sphere (Figure 11c full line) is explained, as for silver, by interface damping,[78,79] shape distribution, and mode mixing between $A_{\parallel}$ and $B_{\parallel}$. The analysis of the t-power law behavior of ω_j in a range where the oscillator strength F_j/t is nearly constant (t > 1.3 nm) leads to $D \propto D^{0.7\pm0.1}$. This size scaling, consistent with previous studies,[43,59,60] matches the dynamic coalescence of silver on alumina ($D \propto D^{0.65\pm0.1}$).

Gold on Titania: Image Field Effect and Band Bending. The inverted Im(γ) term of Au/titania (Figure 9c) shares similarities with that of Au/alumina. However, the inversion fails to recover the Im(β) term because of a series of difficulties involving (i) the ISs intertwining, (ii) the dielectric function of the substrate, in particular above the band gap absorption threshold (see Figure 2 of ref 30), and (iii) the huge relative intensity of the parallel and perpendicular ISs below 3 eV.[30] Simulations (Figure 10c,d) were performed by modeling particles by truncated spheres and by using shape identical to that of Ag and Au/alumina on the basis of earlier near-field or

dx.doi.org/10.1021/jp500675h | J. Phys. Chem. C 2014, 118, 7032−7048

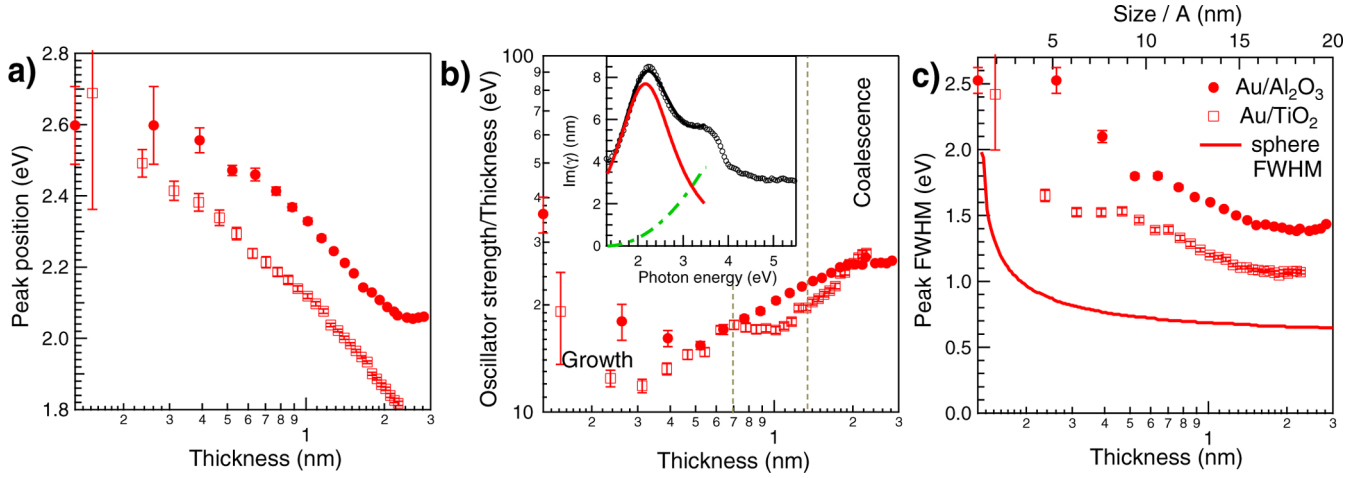

Figure 11. Evolution during growth for the Au/alumina (circle) and Au/titania (square) of (a) the position ω_j, (b) the integrated oscillator F_j normalized by the film thickness, and (c) the peak fwhm of the main component of Im(γ). The decomposition with only one oscillator (continuous red line) and a parabolic background (green dash dotted line) is shown in inset of part b for the 1 nm Au/alumina thick deposit of Figure 8. The peak fwhm is compared to the expected size dependence fwhm of the unsupported Au full sphere (top scale). Vertical dotted lines in part b highlight the transition from growth to coalescence.

electron microscopies[80,81] and X-ray diffuse scattering[59] findings. Regarding Im(γ), the model predicts an overwhelming $A_{\parallel}$ mode around 1.9 eV and less intense $B_{\parallel}$ and $C_{\parallel}$ modes around 2.5 and 2.3 eV, respectively (Figure 10c). The energy splitting due to image field is higher than on alumina due to the dielectric constant difference between the two substrates (a factor 2) in that spectral range[44] (see Figure 2 of ref 30). This takes away $A_{\parallel}$ resonance frequency from interband transition and enhances its intensity compared to the alumina substrate. At variance, the gold interband transition washes out modes other than $A_{\parallel}$ although being still located in the band gap of titania. The main component of the simulated Im(β) IS is A_z (Figure 10) even when the whole absorption is taken into account in the gold dielectric function.

Unlike Au/alumina, the experimental peak shifting between 2.5 and 1.8 eV can be safely assigned to the isolated plasmon absorption $A_{\parallel}$. However, dielectric simulations (Figure 10c,d) fail to reproduce the Im(γ) feature around 4.2 eV whose intensity increases with coverage (Figure 9c). Similarities with the dielectric function of titania (Figure 9d, bold line) and the absence of this feature in the case of the wide band gap alumina suggest to assign it to modifications of the absorption across the band gap of titania by gold. Defective and vacuum-reduced titania shows band bending[82] due to the gradient of defects between surface and bulk.[82−88] Extra electrons due to surface defects such as oxygen vacancies act as donors toward the bulk of the crystal.[85,87] The induced surface dipole directed outward bends bands downward by few tenths of an electronvolt depending on the reduction state[85] (Figure 11), creates an accumulation layer since the Fermi level is closer to the conduction band,[89] and lowers the work function of TiO_2.[85,87] As seen in photoemission, the deposition of gold on titania induces a charge transfer between the metal and the surface defects.[84,85,88,90,91] Its sign varies with the reduction state[84,85,88,90,91] because work functions of gold ($W_{Au} \simeq 5.4$ eV) and TiO_2 ($W_{TiO_2} \simeq 4.6-5.4$ eV) are close from each other.[85,87] Anyway, gold affects the band bending by a fraction of electronvolt,[83−85,87] which induces on the optical properties a similar effect as that observed in electroreflectance experiments.[92] Indeed, the derivative of the dielectric function of titania $-\mathrm{dIm}(\epsilon_{TiO2})/\mathrm{d}\hbar\omega$ shows features similar to the experimental spectra[92] (Figure 9d). An estimate of the thickness affected by the phenomenon is given by the space charge model in the Schottky limit:[82,93]

$$L_{BB} = \sqrt{\frac{2\epsilon_r\epsilon_0 V_{BB}}{eN_d}} \tag{6}$$

where $\epsilon_r \simeq 7$ is the static dielectric function of TiO_2, $V_{BB} \simeq 0.2-0.3$ eV the band bending due to surface defects, and N_d their density. Resistivity measurements[94] and thermodynamic calculations[95] give $N_d \simeq 3 \times 10^{19}$ cm^{-3} at annealing temperature used herein, $T \simeq 1100$ K. The obtained value $L_{BB} \simeq 2-3$ nm matches the thickness optically affected; indeed in the continuous thin-film picture of ISs,[33] this amounts to $t_{BB} \simeq \mathrm{Im}(\gamma)/(\mathrm{Im}(\epsilon_{TiO_2} - 1) \simeq 1-2$ nm at the gold maximum coverage. However, owing to the 3D growth process and the fractional coverage of the surface by gold, the semi-infinite Schottky limit is only valid in first approximation. Finally, the dominant character of the phenomenon along parallel direction furthers favors a quantum-well absorption. A similar band bending may explain the observed kink around 3.2 eV in the optical response of Ag/ZnO (Figure 3c).

In contrast with alumina whose modes $A_{\parallel}$ and $B_{\parallel}$ are intertwined, the simulation fully justifies the representation of the low energy part of Im(γ) of Au/titania by a unique ($A_{\parallel}$ mode) oscillator with a parabolic background term. Oscillator parameters, i.e. position, strength, and fwhm, are compared with those of Au/alumina (Figure 11). A more pronounced shift in energy is found, as expected from a basic argument of stronger image dipole field.[8,12] The change in behavior of the oscillator strength around $t = 0.7$ nm parallels the transition from growth to coalescence which is accompanied by a slight particle dewetting as observed with grazing incidence diffuse X-ray scattering.[59] Power law analysis ($t > 0.7$ nm) of peak position leads to $D \propto D^{0.7\pm0.1}$, a value close to previous findings ($D \propto D^{0.55\pm0.1}$).

dx.doi.org/10.1021/jp500675h | J. Phys. Chem. C 2014, 118, 7032−7048

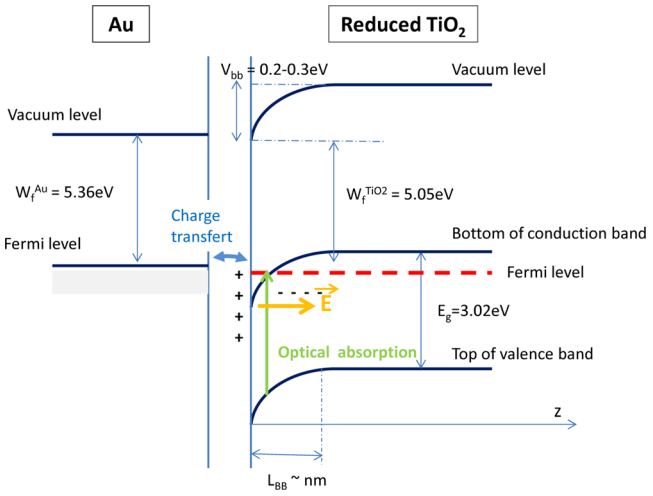

Figure 12. Schematic band diagram before contact between Au and reduced TiO_2. The charge transfer between gold and the surface defects modifies the band bending and modulates the electric field in the space charge layer of nanometric thickness. Numerical values are extracted from ref 85.

PLASMONICS OF INTERBAND TRANSITIONS IN ZINC

The optical response of growing Zn/alumina in both s- and p-polarizations (Figure 13a,b) is dominated by a band around 3.2 eV which lies within the high-energy tail of zinc interband transitions (Figure 1c of Supporting Information). The inversion process is stable for all thicknesses. The lower broadening of p-polarization band stems from the cancellation of Im(γ) and Im(β) terms between 3.7 and 4.5 eV (see eq 5 of ref 30). In the absence of reference about the shape of Zn/alumina particles, a study of the morphology was performed via a quantitative analysis of the optical data to provide a basis to analyze ISs. First, by comparison with the dielectric simulation of a continuous film (Figure 13a,b, thick line), the profile of spectra demonstrates a Volmer–Weber growth even at 100 K. By fitting the SDRS spectrum in p-polarization of the 2.1 nm thick film with a truncated oblate spheroidal shape[11] and accounting for polydisperdity,[42,43] values of size, aspect ratio, and particle density were determined (Figure 13b). The surface coverage was found close to 50%, the in-plane size close to 20 nm, and the fwhm of the fitted inhomogeneous broadening $\sigma_{\parallel}$(fwhm) = 1.2 eV and σ_z(fwhm) = 0.2 eV.[42] The particle shape is shown in Figure 14c,d, and the fit results in Figure 13. Starting from this morphology, simulations of ISs (Figure 14a,b) have been performed with either the full dielectric function of zinc (full line) or the interband contributions only

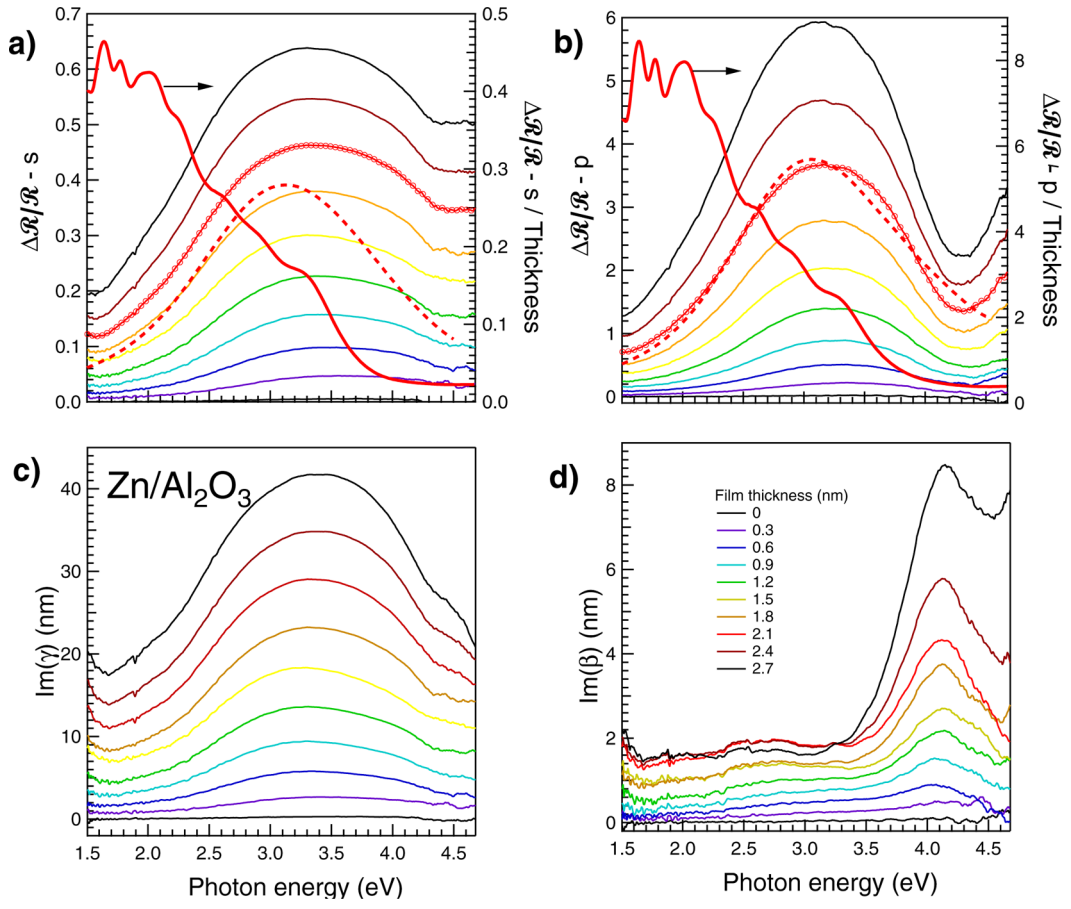

Figure 13. Zinc on alumina: same legend as for Figure 2. In parts a and b, calculated SDRS of a thin continuous film after normalization by the film thickness (thick line; right scale) is compared to the data. Fits of the 2.1 nm SDRS spectra (circles) have been added as thick dotted lines in parts a and b. Modeling (see text) has been performed with a truncated oblate spheroidal shape. Notice that the contribution of the perpendicular IS β is hardly discernible in the p-polarization spectra.

dx.doi.org/10.1021/jp500675h | J. Phys. Chem. C 2014, 118, 7032–7048

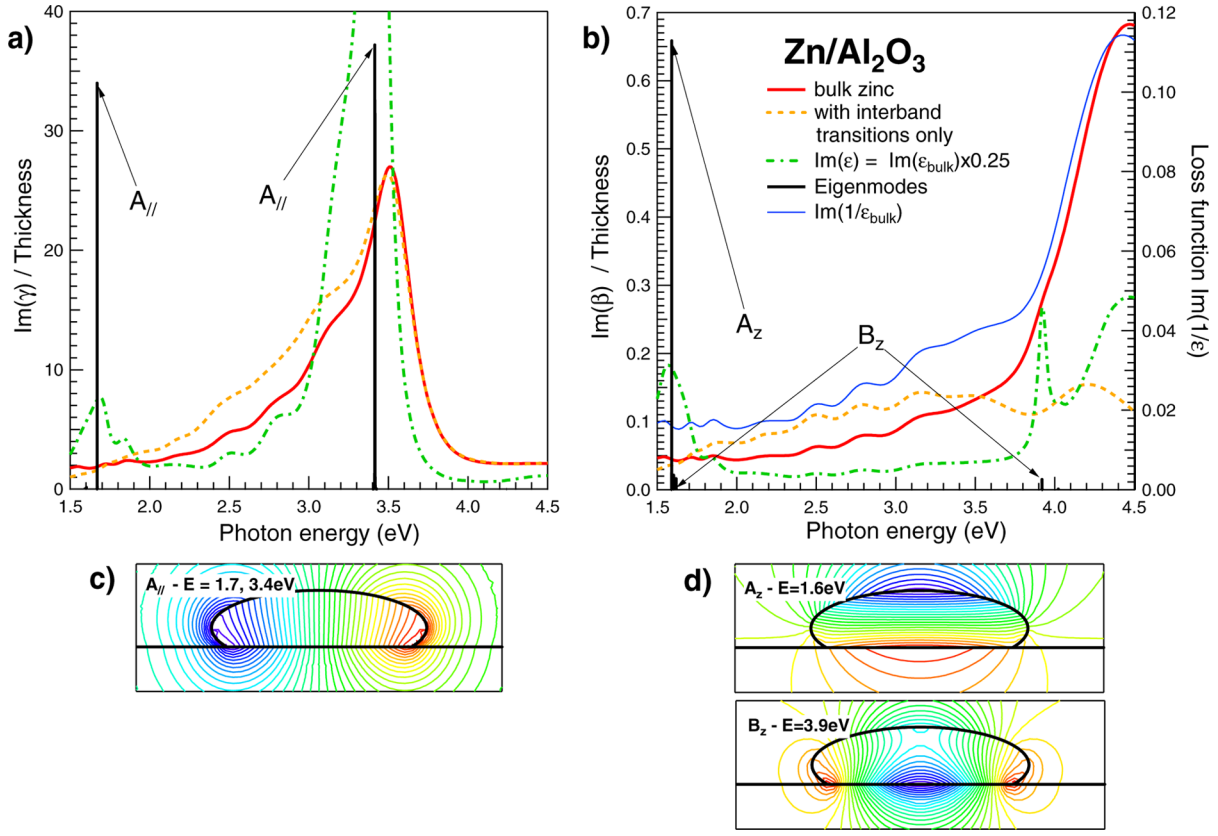

Figure 14. Zinc on alumina: simulated imaginary parts of (a) the parallel γ and (b) perpendicular β IS for a truncated oblate spheroid shape shown in parts c and d. The simulations have been run with (i) the whole bulk dielectric function of zinc (full red line), with (ii) the interband transition component only (dotted orange line) accordingly to the decomposition of Figure 1c of Supporting Information, and with (iii) only 25% of the bulk value (dash-dotted green line). Predicted frequencies and integrated intensities of the eigenmodes of charge vibration are shown as black ticks in parts a and b on an arbitrary scale. The corresponding potential maps are shown in parts c and d. Im(β) is compared to the bulk loss function (thin blue line, left scale) in part b.

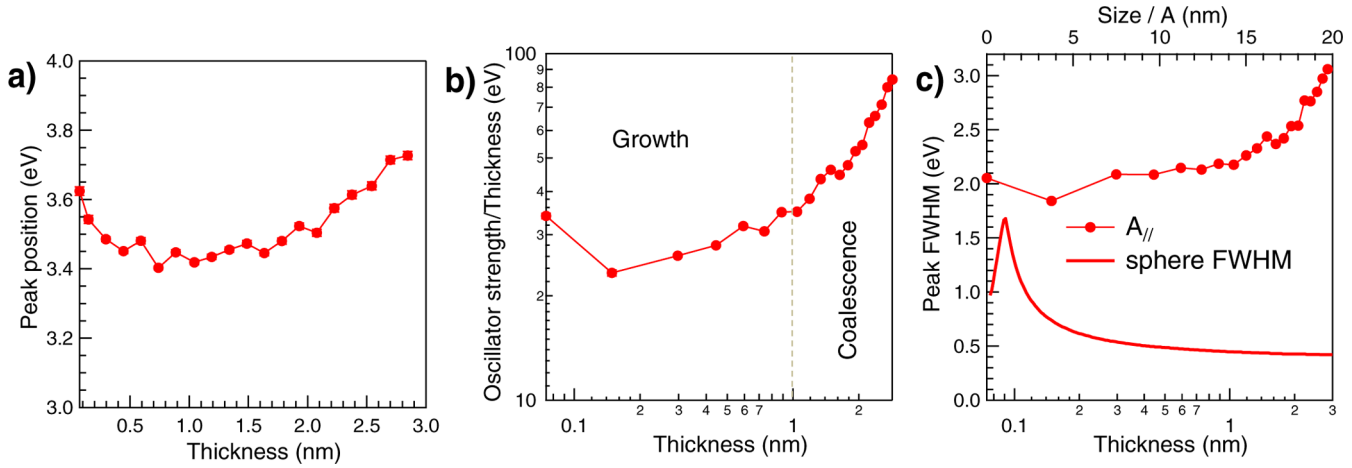

Figure 15. Zinc on alumina: same legend as for Figure 11. Only one component corresponding to $A_{\|}$ mode (filled circles) has been used in the oscillator decomposition of γ-IS. In part c, the fwhm of the band is compared to that of the Frölich mode of the full sphere (top scale). Vertical dotted line in part b highlights the transition from growth to coalescence.

(dotted line), or by taking only a fraction of the bulk dielectric function (dash-dotted line), or by setting the imaginary part of the metal dielectric function close to zero (bars). Five main modes should be excited in the undamped metal: two along the parallel direction at 1.7 and 3.4 eV but of the same nature and three along the normal direction at 1.59, 1.62, and 3.9 eV (ticks in Figure 14a,b). Potential maps (Figure 14c,d) justify the choice of labels $A_{\|}$, A_z, and B_z, by comparison with silver and gold films. In contrast with gold and silver, the excitation of two $A_{\|}$ and two B_z modes in zinc lies in the nonbijective relation between Re(ϵ_{Zn}) and the photon energy (see Supporting Information, Figure 1c). On the contrary, the twin mode of the low-energy A_z does not exist. However, the strong damping due to zinc interband transition entails the extinction of most

dx.doi.org/10.1021/jp500675h | J. Phys. Chem. C 2014, 118, 7032−7048

modes, in particular around 1.6 eV near the maximum of absorption. The mode $A_{\parallel}$ at 3.4 eV is still observed since it lies in a spectral range where $\mathrm{Im}(\epsilon_{Zn})$ is low enough, although the continuous decrease of $\mathrm{Im}(\epsilon_{Zn})$ between 1.5 and 4 eV induces an asymmetry and a shift of the $\mathrm{Im}(\gamma)$ band. Moreover the similarity between $\mathrm{Im}(\gamma)$ calculated with the full dielectric function and that obtained with only the interband transition (Figure 14a) is indicative of a marginal contribution of free electrons or, in other words, a $A_{\parallel}$ resonant "plasmon" mode dominated by bound electrons. In the perpendicular direction, the weak $\mathrm{Im}(\beta)$ feature centered around 4.5 eV is clearly nonresonant. Its similarity with the calculated loss function (Figure 1 of Supporting Information, thin line in Figure 14) shows its bulk character. Therefore, although polarization modes linked to the particle geometry are similar in nature, the case of zinc is drastically different from that of silver and gold for which resonant modes are excited on the free-electron component of the dielectric function (dotted lines in Figure 10 for gold).

The qualitative comparison between experimental ISs of Figure 13c,d and the dielectric simulations (Figure 14a,b) allows assigning the broad feature of $\mathrm{Im}(\gamma)$ to $A_{\parallel}$ and the 4 eV $\mathrm{Im}(\beta)$ to bulk absorption. Fitting $\mathrm{Im}(\gamma)$ with only one oscillator with a parabolic background (not shown) leads to a two-step behavior in the evolution of the parameters ω_j, F_j, and Γ_j (Figure 15). Below ~1 nm, the mode slightly red-shifts at nearly constant strength F_j/t and constant width; above, it is blue-shifted with sizable increase in F_j/t and broadening. Since the higher F_j/t the flatter the particle, this observation can be ascribed to an initial growth at nearly constant shape followed by coalescence with an kinetic hindrance of particle reshaping due to the low temperature, as previously observed for Ag/Al_2O_3 grown either at low temperature[43] or in fast deposition conditions.[54] Although the power law analysis developed with the other metals is hampered by data scattering, information can be drawn from the analysis of the oscillator parameters. The initial red-shift is predicted by eq 3 for a parallel mode (minus sign). Above 1 nm, the expected red-shift due to the increase of F_j is clearly balanced out by a reduction of particle density to lead to an apparent slight blue-shift (eq 3), which confirms the transition toward coalescence. Regarding peak width, the extra broadening of ~1.5 eV during growth (below 1 nm; Figure 15c) relative to the Frölich mode of a full sphere in a high-size limit (~0.42 eV) points to the major role of shape polydispersity over the finite-size effect because of the sensitivity of the $A_{\parallel}$ mode to flattening. However, in contrast to silver and gold (Figures 7c and 11c), peak broadening increases during the coalescence which is consistent with the hypothesized hindrance of particle reshaping upon coalescence (out equilibrium coalescence), which favors shape polydispersity.

INTERFACIAL SUSCEPTIBILITIES AND SUM RULES

Beyond any Kramers–Heisenberg decomposition (eq 1), ISs which describe intrinsically the dielectric behavior of the interface should fulfill sum rules derived from the Kramers–Kronig link[51] between real and imaginary parts. At frequencies higher than any characteristic light absorption threshold, interface susceptibilities are dominated by the inertial effects and not anymore by restoring or dissipative force. Their asymptotic limits should be given by

$$\lim_{\omega\to+\infty} \mathrm{Re}[\gamma(\omega)] \simeq -t\frac{{\omega_p}^2(\gamma)}{\omega^2}$$
$$\lim_{\omega\to+\infty} \mathrm{Re}[\beta(\omega)] \simeq -t\frac{{\omega_p}^2(\beta)}{\omega^2} \quad (7)$$

where $\omega_p(\gamma)$ and $\omega_p(\beta)$ have the meaning of plasma frequencies related to the number of effective electrons involved[51] and t is the interface or film physical thickness. Within the reasonable assumption that $\mathrm{Im}(\gamma)$ and $\mathrm{Im}(\beta)$ fall off faster than ω^{-2} (which is the case for damped oscillator as in eq 1), the high-frequency limit of the Kramers–Kronig relations

$$\mathrm{Re}[\gamma(\omega)] = \frac{2}{\pi}\mathcal{P}\int_0^{+\infty} \mathrm{d}\omega' \frac{\omega'\mathrm{Im}[\gamma(\omega')]}{\omega'^2-\omega^2}$$
$$\mathrm{Re}[\gamma(\beta)] = \frac{2}{\pi}\mathcal{P}\int_0^{+\infty} \mathrm{d}\omega' \frac{\mathrm{Im}[\beta(\omega')]}{\omega'^2-\omega^2} \quad (8)$$

lead to the so-called f-sum rules for ISs:

$${\omega_p}^2(\gamma) = \frac{2}{\pi t}\int_0^{+\infty} \omega\ \mathrm{Im}[\gamma(\omega)]\ \mathrm{d}\omega$$
$${\omega_p}^2(\beta) = \frac{2}{\pi t}\int_0^{+\infty} \omega\ \mathrm{Im}[\beta(\omega)]\ \mathrm{d}\omega \quad (9)$$

The experimental plasma frequencies $\omega_p(\gamma)$ obtained from eq 9 for the four studied interfaces (Ag, Au, Zn/Al_2O_3, Ag/ZnO, Au/TiO_2) and applied to the available spectral range are shown in Figure 16 and compared to values expected from tabulated bulk dielectric constants, i.e., $\omega^2_{p,\mathrm{bulk}}(\gamma) = (2/\pi)\int_0^{+\infty}\omega\ \mathrm{Im}[\epsilon(\omega)]\ \mathrm{d}\omega$, which correspond to the continuous thin film limit of ISs.[33] Because of inversion pitfalls,[30] such a sum rule analysis is less reliable for the perpendicular IS and loss function, in particular for gold. A nearly constant value $\omega_p(\gamma)$ is found in the limit of

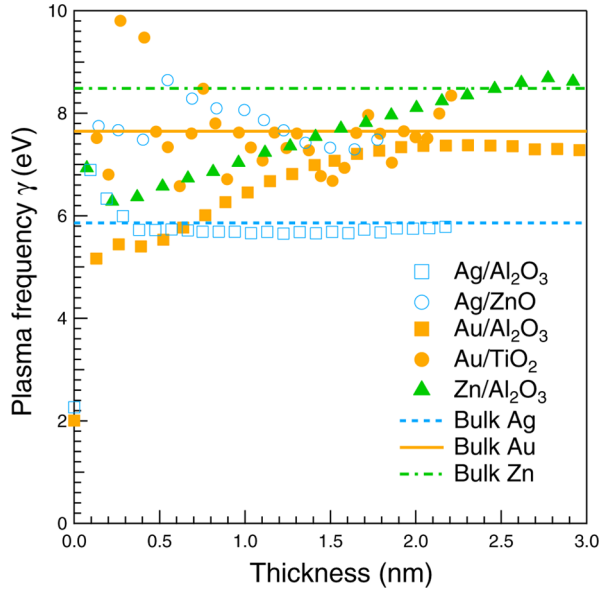

Figure 16. Plasma frequency $\omega_p(\gamma)$ obtained from sum rule applied to parallel IS of all the studies interfaces: Ag/Al_2O_3 (open blue squares), Ag/ZnO (open blue circles), Au/Al_2O_3 (filled orange squares), Au/TiO_2 (filled orange circles), Zn/Al_2O_3 (filled green triangles). Expected values from bulk dielectric constants are shown for Ag (dotted blue line), Au (orange continuous line), and Zn (green dash-dotted line).

dx.doi.org/10.1021/jp500675h | J. Phys. Chem. C 2014, 118, 7032–7048

the thickest films since the UV−vis spectral range encompasses most of the plasmon resonances of the nanoparticles. Since the sum rule analysis also includes interband absorptions and substrate contributions, the agreement with the bulk behavior validates *a posteriori* the inversion process[30] which should fulfill electron conservation.

CONCLUSIONS AND OUTLOOK

Surface differential reflectivity spectroscopy was used to monitor the plasmonic response of growing Ag, Au, Zn/alumina, Ag/zincite, and Au/titania nanoparticles. The parallel and perpendicular components of the interfacial susceptibilities which characterize the dielectric behavior of the film are deconvoluted from the substrate contribution by using a previously proposed algorithm of inversion of the reflection coefficients which clarifies the reading of the film parameters. A combination of Kramers−Heisenberg decomposition of ISs in terms of damped oscillators and of dielectric simulations based on truncated spheres or spheroids demonstrates the universality of the observed plasmon modes for supported nanoparticles. A close comparison between the three metals, which have similar Drude dielectric behaviors, highlights the paramount role of the metal interband absorption in the visibility of the various features. While with silver and gold the localized plasmon excitation involve free electrons, zinc develops polarization modes on the tail of the interband absorption. The comparison between the studied interfaces allowed discussing shape, image field, polydispersity, interband absorption, and interface damping effects in the evolution of frequencies, oscillator strengths, and broadenings of the modes. In particular, power law behavior of the size evolution could be deduced from the frequency shift in the coalescence regime. For semiconducting substrates, the observed metal induced gap absorption was assigned to charge transfer and evolution of band bending at the metal/oxide interface. Monitoring of growth processes and gas adsorption are obvious perspectives for the application for such an approach of the plasmon modes in supported nanoparticles.

ASSOCIATED CONTENT

Supporting Information

Method to account for interband contributions in the interfacial susceptibilities as well as the used dielectric functions and their decomposition into bound and free electron components. This material is available free of charge via the Internet at http://pubs.acs.org.

AUTHOR INFORMATION

Corresponding Author

*E-mail: remi.lazzari@insp.jussieu.fr (R.L.).

Notes

The authors declare no competing financial interest.

ACKNOWLEDGMENTS

R.L. acknowledges the technical assistance of S. Chenot and H. Cruguel (INSP) as well the help of M. de Grazia (Saint-Gobain Recherche) and J. Li (INSP) during some SDRS experiments. This work has been supported by ANR (Agence Nationale de la Recherche) (Program "Matériaux et Procédés pour des Produits Performants", contract ANR-2011-RMNP-010, CO-COTRANS) and has benefited from a mobility grant AURORA between France and Norway. The PhD thesis of R.C. was sponsored by Arcelor-Mittal and ANRT (Association Nationale de la Recherche et de la Technologie). The research of I.S. was supported in part by the RCN (Research Council of Norway, Contract No. 216699).

REFERENCES

(1) Bohren, C. F.; Huffman, D. R. In *Absorption and Scattering of Light by Small Particles*; John Wiley & Sons: New York, 1983.
(2) Kreibig, U.; Vollmer, M. *Optical Properties of Metal Clusters*; Springer Series in Material Science; Springer Verlag: Berlin, 1995; Vol. *25*.
(3) Noguez, C. Surface plasmons on metal nanoparticles: The influence of shape and physical environment. *J. Phys. Chem. C* **2007**, *111*, 3806−3819.
(4) Rycenga, M.; Cobley, C. M.; Zeng, J.; Li, W.; Moran, C. H.; Zhang, Q.; Qin, D.; Xia, Y. Controlling the synthesis and assembly of silver nanostructures for plasmonic applications. *Chem. Rev.* **2011**, *111*, 3669−3712.
(5) Mie, G. Beitrage zur optik trüber medien speziell kolloidaler metallösungen. *Ann. Phys.* **1908**, *25*, 377−445.
(6) Román-Velázquez, C. E.; Noguez, C.; Barrera, R. G. Substrate effects on the optical properties of spheroidal nanoparticles. *Phys. Rev. B* **2000**, *61*, 10427−10436.
(7) Nordlander, P.; Prodan, E. Plasmon hybridization in nanoparticles near metallic surfaces. *Nano Lett.* **2004**, *11*, 2209−2213.
(8) Knight, M. W.; Wu, Y.; Lassiter, J. B.; Nordlander, P.; Halas, N. J. Substrates matter: influence of an adjacent dielectric on an individual plasmonic nanoparticle. *Nano Lett.* **2009**, *9*, 2188−2192.
(9) Lermé, J.; Bonnet, C.; Broyer, M.; Cottancin, E.; Manchon, D.; Pellarin, M. Optical properties of a particle above a dielectric interface: cross sections, benchmark calculations, and analysis of the intrinsic substrate effects. *J. Phys. Chem. C* **2013**, *117*, 6383−6398.
(10) Simonsen, I.; Lazzari, R.; Jupille, J.; Roux, S. Numerical modelling of the optical response of supported metallic particles. *Phys. Rev. B* **2000**, *61*, 7722−7733.
(11) Lazzari, R.; Simonsen, I.; Bedeaux, D.; Vlieger, J.; Jupille, J. Polarizability of truncated spheroidal island supported by a substrate: models and applications. *Eur. Phys. J. B* **2001**, *24*, 267−284.
(12) Lazzari, R.; Roux, S.; Simonsen, I.; Jupille, J.; Bedeaux, D.; Vlieger, J. Multipolar optical absorptions in supported metallic particles: the case of $Ag/Al_2O_3(0001)$. *Phys. Rev. B* **2002**, *65*, 235424−1.
(13) Albella, P.; Garcia-Cueto, B.; Gonzalez, F.; Moreno, F.; Wu, P. C.; Kim, T. H.; Brown, A.; Yang, Y.; Everitt, H. O.; Videen, G. Shape matters: plasmonic nanoparticle shape enhances interaction with dielectric substrate. *Nano Lett.* **2011**, *11*, 3531−3537.
(14) Beita, C.; Borensztein, Y.; Lazzari, R.; Nieto, J.; Barrera, R. Substrate-induced multipolar resonances in supported free-electron metal spheres. *Phys. Rev. B* **1999**, *60*, 6018−6022.
(15) Aubry, A.; Lei, D. Y.; Maier, S. A.; Pendry, J. B. Plasmonic hybridization between nanowires and a metallic surface: a transformation optics approach. *ACS Nano* **2011**, *5*, 3293−3308.
(16) Pinchuk, A.; Hilger, A.; von Plessen, G.; Kreibig, U. Substrate effect on the optical response of silver nanoparticles. *Nanotechnology* **2004**, *15*, 1890−1896.
(17) Dmitriev, A.; Hägglund, C.; Chen, S.; Fredriksson, H.; Pakizeh, T.; Käll, M.; Sutherland, D. Enhanced nanoplasmonic optical sensors with reduced substrate effect. *Nano Lett.* **2008**, *8*, 13893−3898.
(18) Mock, J. J.; Hill, R. T.; Degiron, A.; Zauscher, S.; Chilkoti, A.; Smith, D. R. Distance-dependent plasmon resonant coupling between a gold nanoparticle and gold Film. *Nano Lett.* **2008**, *8*, 2245−2252.
(19) Vernon, K. C.; Funston, A. M.; Novo, C.; Gómez, D. E.; Mulvaney, P.; Davis, T. J. Influence of particle-substrate interaction on localized plasmon resonances. *Nano Lett.* **2010**, *10*, 2080−2086.
(20) Chen, H.; Shao, L.; Ming, T.; Woo, K. T.; Man, Y. C.; Wang, J.; Lin, H. Q. Observation of the Fano resonance in gold nanorods supported on high-dielectric-constant substrates. *ACS Nano* **2011**, *5*, 6754−6763.

(21) Letnes, P.; Simonsen, I.; Mills, D. Substrate influence on the plasmonic response of clusters of spherical nanoparticles. *Phys. Rev. B* **2011**, *83*, 075426.
(22) Hilger, A.; Tenfelde, M.; Kreibig, U. Silver nanoparticles deposited on dielectric surfaces. *Appl. Phys. B: Laser Opt.* **2001**, *73*, 361−372.
(23) Kreibig, U. Interface-induced dephasing of Mie plasmon polaritons. *Appl. Phys. B: Laser Opt.* **2008**, *93*, 79−89.
(24) Lazzari, R.; Layet, J. M.; Jupille, J. Electron-energy-loss channels and plasmon confinement in supported silver particles. *Phys. Rev. B* **2003**, *68*, 045428.
(25) Swanglap, P.; Slaughter, L. S.; Chang, W.-S.; Willingham, B.; Khanal, B. P.; Zubarev, E. R.; Link, S. Seeing double: coupling between substrate image charges and collective plasmon modes in self-assembled nanoparticle superstructures. *ACS Nano* **2011**, *5*, 4892−4901.
(26) Zhao, J.; Pinchuk, A.; Mc. Mahon, J. M.; Li, S.; Ausman, L. K.; Atkinson, A. L.; Schatz, G. C. Methods for describing the electromagnetic properties of silver and gold nanoparticles. *Acc. Chem. Res.* **2008**, *41*, 1710−1720.
(27) Myroshnychenko, V.; Rodríguez-Fernández, J.; Pastoriza-Santos, I.; Funston, A. M.; Novo, C.; Mulvaney, P.; Liz-Marzán, L. M.; García de Abajo, F. J. Modelling the optical response of gold nanoparticles. *Chem. Soc. Rev.* **2008**, *37*, 1792−1805.
(28) Proehl, H.; Nitsche, R.; Dienel, T.; Leo, K.; Fritz, T. *In situ* differential reflectance spectroscopy of thin crystalline films of PTCDA on different substrates. *Phys. Rev. B* **2005**, *71*, 165207.
(29) Forker, R.; Gruenewald, M.; Fritz, T. Optical differential reflectance spectroscopy on thin molecular films. *Annu. Rep. Prog. Chem., Sect. C: Phys. Chem.* **2012**, *108*, 34−68.
(30) Lazzari, R.; Simonsen, I.; Jupille, J. Interfacial susceptibilities in nanoplasmonics via inversion of Fresnel coefficients. *Plasmonics* **2013**, DOI10.1007/s11468-013-9619-6.
(31) Bedeaux, D.; Vlieger, J. A phenomenological theory of the dielectric properties of thin films. *Physica* **1973**, *67*, 55−73.
(32) Haarmans, M.; Bedeaux, D. Optical properties of thin films up to second order in the thickness. *Thin Solid Films* **1995**, *258*, 213−223.
(33) Bedeaux, D.; Vlieger, J. *Optical Properties of Surfaces*; Imperial College Press: London, 2001.
(34) Yamaguchi, T.; Ogawa, M.; Takahashi, H.; Saito, N. Optical absorption of submonoloayer silver films: size dependence of.in small island particles. *Surf. Sci.* **1983**, *129*, 232−246.
(35) Pakizeh, T.; Langhammer, C.; Zorić, I.; Apell, P.; Käll, M. Intrinsic Fano interference of localized plasmons in Pd nanoparticles. *Nano Lett.* **2009**, *9*, 882−886.
(36) Pakizeh, T. Optical absorption of plasmonic nanoparticles in presence of a local interband transition. *J. Phys. Chem. C* **2011**, *115*, 21826−21831.
(37) Little, S. A.; Collins, R. W.; Marsillac, S. Analysis of interband, intraband, and plasmon polariton transitions in silver nanoparticle films via *in situ* real-time spectroscopic ellipsometry. *Appl. Phys. Lett.* **2011**, *98*, 101910.
(38) Little, S. A.; Begou, T.; Collins, R. W.; Marsillac, S. Optical detection of melting point depression for silver nanoparticles via.*in situ* real time spectroscopic ellipsometry. *Appl. Phys. Lett.* **2012**, *100*, 051107.
(39) Bagchi, A.; Barrera, R.; Fuchs, R. Local-field effect in optical reflectance from adsorbed overlayers. *Phys. Rev. B* **1982**, *25*, 7086−7096.
(40) Bergman, D. J. The dielectric constant of composite material: a problem in classical physics. *Phys. Rep.* **1978**, *43*, 377−407.
(41) Lazzari, R.; Simonsen, I.; Jupille, J. Onset of charge localisation on coupling multipolar absorption modes in supported silver particles. *Europhys. Lett.* **2003**, *61*, 541−546.
(42) Lazzari, R.; Jupille, J. Quantitative analysis of nanoparticle growth through plasmonics. *Nanotechnology* **2011**, *22*, 445703.
(43) Lazzari, R.; Jupille, J. Growth kinetics and size-dependent wetting of Ag/α-Al_2O_3(0001) nanoparticles studied via the plasmonic response. *Nanotechnology* **2012**, *23*, 135707−135720.
(44) Palik, E. D. *Handbook of Optical Constants of Solids*; Academic Press: New York, 1985; Vols. *1*−*3*.
(45) Johnson, P.; Christy, R. Optical constant of noble metals. *Phys. Rev. B* **1972**, *6*, 4370−4379.
(46) Stahrenberg, K.; Herrmann, T.; Wilmers, K.; Esser, N.; Richter, W.; Lee, M. J. G. Optical properties of copper and silver in the energy range 2.5−9.0 eV. *Phys. Rev. B* **2001**, *64*, 115111−1.
(47) Nash, D. J.; Sambles, J. R. Surface plasmon-polariton study of the optical dielectric function of zinc. *J. Mod. Opt.* **1998**, *45*, 2585−2596.
(48) Jellison, G. E.; Batner, L. A. Optical functions of uniaxial ZnO determined by generalized ellipsometry. *Phys. Rev. B* **1998**, *58*, 3586−3589.
(49) Lazzari, R.; Simonsen, I. GranFilm: a software for calculating thin-layer dielectric properties and Fresnel coefficients. *Thin Solid Films* **2002**, *419*, 124−136.
(50) GranFilm can be downloaded with an user guide from http://ln-www.insp.upmc.fr/axe4/Oxydes/GranFilm/GranularFilm.html.
(51) Smith, D. In *Handbook of Optical Constants of Solids*; Palik, E. D., Ed.; Academic Press: New York, 1985; Vol. *1*, Chapter Dispersion theory, sum rules and their applications in the analysis of optical data, pp 35−64.
(52) Rodriguez, J. A.; Kuhn, M.; Hrbek, J. Interaction of silver, cesium, and zinc with alumina surfaces: thermal desorption and photoemission studies. *J. Phys. Chem.* **1996**, *100*, 18240−18248.
(53) Wind, M. M.; Vlieger, J. The polarizability of a truncated sphere on a substrate I. *Physica A* **1987**, *141*, 33−57.
(54) Grachev, S.; de Grazia, M.; Barthel, E.; Søndergård, E.; Lazzari, R. Real time monitoring of nanoparticle film growth at high deposition rate with optical spectroscopy of plasmon resonances. *J. Phys. D: Appl. Phys.* **2013**, *46* (10), 375305.
(55) Lazzari, R.; Jupille, J. Silver layers on oxide surfaces: morphology and optical properties. *Surf. Sci.* **2001**, *482*−*485*, 823−827.
(56) Jedrecy, N.; Renaud, G.; Lazzari, R.; Jupille, J. Flat-top silver nanocrystals on the two polar faces of ZnO: an all angle X-ray scattering investigation. *Phys. Rev. B* **2005**, *72*, 045430.
(57) Jedrecy, N.; Renaud, G.; Lazzari, R.; Jupille, J. Unstrained islands with interface coincidence sites versus strained islands: X-ray measurements on Ag/ZnO. *Phys. Rev. B* **2005**, *72*, 195404.
(58) Lazzari, R.; Jupille, J. Interfacial chemistry and wetting of metallic films on the hydroxylated α-Al_2O_3(0001) surface. *Phys. Rev. B* **2005**, *71*, 045409.
(59) Lazzari, R.; Leroy, F.; Renaud, G.; Jupille, J. Self-similarity during growth of the Au/TiO_2(110) model catalyst as seen by grazing incidence X-ray scattering techniques. *Phys. Rev. B* **2007**, *76*, 125412.
(60) Revenant, C.; Renaud, G.; Lazzari, R.; Jupille, J. Defect-pinned nucleation, growth, and dynamic coalescence of Ag islands on MgO(001): an *in situ* grazing-incidence small-angle X-ray scattering study. *Phys. Rev. B* **2009**, *79*, 235424.
(61) Meakin, P. Droplet deposition, growth and coalescence. *Rep. Prog. Phys.* **1992**, *55*, 157−240.
(62) Beysens, D. Dew nucleation and growth. *C. R. Phys.* **2006**, *7*, 1082−1100.
(63) Hövel, H.; Fritz, S.; Hilger, A.; Kreibig, U.; Vollmer, M. Width of cluster plasmon resonances: bulk dielectric functions and chemical interface damping. *Phys. Rev. B* **1993**, *48*, 18178−18188.
(64) Persson, B. N. J. Polarizability of small spherical metal particles: influence of the matrix environment. *Surf. Sci.* **1993**, *281*, 153−162.
(65) Bosbach, J.; Hendrich, C.; Stietz, F.; Vartanyan, T.; Träger, F. Ultrafast dephasing of surface plasmon excitation in silver nanoparticles: influence of particle size, shape and chemical surrounding. *Phys. Rev. Lett.* **2002**, *89*, 257404.
(66) Kreibig, U.; Fragstein, C. The limitation of electron mean free path in small silver particles. *Z. Phys.* **1969**, *224*, 307−323.
(67) Kreibig, U. Anomalous frequency and temperature dependence of the optical absorptions of small gold particles. *J. Phys. F* **1977**, *38*, 97−103.
(68) Kraus, W. A.; Schatz, G. C. Plasmon resonance broadening in small metal particles. *J. Chem. Phys.* **1983**, *79*, 6130−6139.

(69) Kreibig, U.; Genzel, L. Optical absorption of small metallic particles. *Surf. Sci.* **1985**, *156*, 678−700.
(70) Coronado, E.; Schatz, G. Surface plasmon broadening for arbitrary shape nanoparticles: a geometrical probability approach. *J. Chem. Phys.* **2003**, *119*, 3926−3934.
(71) Kreibig, U. Small silver particles in photosensitive glass: their nucleation and growth. *Appl. Phys.* **1976**, *10*, 255−263.
(72) Etchegoin, P. G.; Le Ru, E. C.; Meyer, M. An analytic model for the optical properties of gold. *J. Chem. Phys.* **2006**, *125*, 164705.
(73) Chatain, D.; Chabert, F.; Ghetta, V. New experimental setup for wettability characterization under monitored oxygen activity: I Role of oxidation state and defect concentration on oxide wettability by gold. *J. Am. Ceram. Soc.* **1993**, *76*, 1568−1576.
(74) Campbell, C. T. Ultrathin metal films and particles on oxide surfaces: structural, electronic and chemisorptive properties. *Surf. Sci. Rep.* **1997**, *27*, 1−111.
(75) Scaffardi, J. B.; Otocho, J. Size dependence of refractive index of gold nanoparticles. *Nanotechnology* **2006**, *17*, 1309−1315.
(76) Santillán, J. M. J.; Videla, F. A.; Fernández van Raap, M. B.; Schinca, D. C.; Scaffardi, L. B. Size dependent Cu dielectric function for plasmon spectroscopy: Characterization of colloidal suspension generated by fs laser ablation. *J. Appl. Phys.* **2012**, *112*, 054319.
(77) Leng, J.; Opsala, J.; Chua, H.; Senkoa, M.; Aspnes, D. Analytic representations of the dielectric functions of materials for device and structural modeling. *Thin Solid Films* **1998**, *313*−*314*, 132−136.
(78) Berciaud, S.; Cognet, L.; Tamarat, P.; Lounis, B. Observation of intrinsic size effects in the optical response of individual gold nanoparticles. *Nano Lett.* **2005**, *5*, 515−518.
(79) Hubenthal, F. Increased damping of plasmon resonances in gold nanoparticles due to broadening of the band structure. *Plasmonics* **2013**, *8*, 1341−1349.
(80) Lai, X.; St Clair, T.; Valden, M.; Goodman, D. Scanning tunneling microscopies studies of metal clusters supported on TiO_2(110): morphology and electronic structure. *Prog. Surf. Sci.* **1998**, *59*, 25−52.
(81) Cosandey, F.; Madey, T. Growth, morphology and interfacial effects and catalytic properties of Au on TiO_2. *Surf. Rev. Lett.* **2001**, *8*, 73−93.
(82) Zhang, Z.; Yates, J. Y. Band bending in semiconductors: chemical and physical consequences at surfaces and interfaces. *Chem. Rev.* **2012**, *112*, 5520−5551.
(83) Zhang, L.; Persaud, R.; Madey, T. Ultrathin metal films on a metal oxide surface: growth of Au on TiO_2(110). *Phys. Rev. B* **1999**, *73*, 73.
(84) Minato, T.; Susaki, T.; Shiraki, S.; Kato, H. S.; Kawai, M.; Aika, K. I. Investigation of the electronic interaction between TiO_2(1 1 0) surfaces and Au clusters by PES and STM. *Surf. Sci.* **2004**, *566*−*568*, 1012−1017.
(85) Okazawa, T.; Kohyama, M.; Kido, Y. Electronic properties of Au nano-particles supported on stoichiometric and reduced TiO_2(110) substrates. *Surf. Sci.* **2006**, *600*, 4430−4437.
(86) Nowotny, J.; Bak, T.; Sheppard, L. R.; Nowotny, M. K. Reactivity of titanium dioxide with oxygen at room temperature and the related charge transfer. *J. Am. Chem. Soc.* **2008**, *130*, 9984−9993.
(87) Mitsuhara, K.; Kitsudo, Y.; Matsumoto, H.; Visikovskiy, A.; Takizawa, M.; Nishimura, T.; Akita, T.; Kido, Y. Electronic charge transfer between Au nano-particles and TiO_2-terminated $SrTiO_3$(001) substrate. *Surf. Sci.* **2010**, *604*, 548−554.
(88) Zhang, Z.; Tang, W.; Neurock, M.; Yates, J. T. Electric charge of single Au atoms adsorbed on TiO_2(110) and associated band bending. *J. Phys. Chem. C* **2011**, *115*, 23848−23853.
(89) See, A. K.; Bartynski, R. A. Inverse photoemission study of the defective TiO_2(110) surface. *J. Vac. Sci. Technol.* **1992**, *10*, 2591−2596.
(90) Jiang, Z.; Zhang, W.; Jin, L.; Yang, X.; Xu, F.; Zhu, J.; Huang, W. Direct XPS evidence for charge transfer from a reduced rutile TiO_2(110) surface to Au clusters. *J. Phys. Chem. C* **2007**, *111*, 12434−12439.
(91) Dumbuya, K.; Cabailh, G.; Lazzari, R.; Jupille, J.; Ringel, L.; Pistor, M.; Lytken, O.; Steinrück, H.-P.; Gottfried, J. Evidence for an active oxygen species on Au/TiO_2 (110) model catalysts during investigation with.*in situ* X-ray photoelectron spectroscopy. *Catal. Today* **2012**, *181*, 20−25.
(92) Pollak, F. H.; Shen, H. Modulation spectroscopy of semiconductors: bulk/thin film, microstructures, surfaces/interfaces and devices. *Mater. Sci. Eng.* **1993**, *10*, 275−374.
(93) Lüth, H. In *Surface and Interfaces of Solids*; Springer Verlag: Berlin, 1992; Vol. *15*.
(94) Iguchi, E.; Yajima, K.; Asahina, T.; Kanamori, Y. Resistivities of reduced rutile (TiO_2) from 300 K to exhaustion range. *J. Phys. Chem. Solids* **1974**, *35*, 597−599.
(95) Bak, T.; Nowotny, J.; Rekas, M.; Sorrell, C. C. Defect chemistry and semiconducting properties of titanium dioxide: II. Defect diagrams. *J. Phys. Chem. Solids* **2003**, *64*, 1057−1067.